Upper crustal velocity structure beneath the central Lucky Strike Segment from seismic refraction measurements

T. Seher, S.C. Singh, W.C. Crawford, J. Escartin

Geochemistry Geophysics Geosystems G3

Article
Volume 11, Number 5
5 May 2010
Q05001, doi:10.1029/2009GC002894
ISSN: 1525-2027

Published by AGU and the Geochemical Society

Upper crustal velocity structure beneath the central Lucky Strike Segment from seismic refraction measurements

Tim Seher

Géosciences Marines, Institut de Physique du Globe de Paris, Boite 89, 4 place Jussieu, F-75252 Paris CEDEX 05, France (seher@ipgp.fr)

Now at Earth Resources Laboratory, Massachusetts Institute of Technology, Cambridge, Massachusetts 02139, USA

Satish C. Singh, Wayne C. Crawford, and Javier Escartín

Géosciences Marines, Institut de Physique du Globe de Paris, Boite 89, 4 place Jussieu, F-75252 Paris CEDEX 05, France

[1] We present a three-dimensional velocity model of the upper crust around the central volcano of the Lucky Strike Segment, Mid-Atlantic Ridge. The model, constructed from a 3-D array of air gun shots (37.5 m spacing along line and 100 m between lines) to ocean bottom seismometers fired during a 3-D seismic reflection survey, shows an off-axis velocity increase (~1 km/s), a low-velocity region within the median valley, and a low-velocity anomaly underneath the Lucky Strike volcano. Our observations indicate a porosity decrease of 1%–9% (corresponding to a velocity increase of ~0.5–1 km/s) over a distance of 8 km from the ridge axis (~0.7 Ma) and a porosity decrease of 4%–11% (corresponding to a velocity increase of ~2 km/s) between a depth of 0.5 and 1.75 km below seafloor. A sinusoidal variation in the traveltime residuals indicates the presence of azimuthal anisotropy with cracks aligned approximately along the ridge axis. We favor an interpretation in which upper crustal porosities are created by a combination of magmatic accretion (lava–sheeted dike boundary) and active extension (faults, fractures, and fissures). The porosity variation with depth probably depends on pore space collapse, hydrothermal alteration, and a change of stress accommodation. The off-axis porosities are possibly influenced by both hydrothermal precipitation and the aging of the crust.

Components: 12,800 words, 13 figures.

Keywords: Mid-Atlantic Ridge; Lucky Strike; seismic refraction; tomography; oceanic crust.

Index Terms: 3025 Marine Geology and Geophysics: Marine seismics (0935); 7245 Seismology: Mid-ocean ridges; 7220 Seismology: Oceanic crust.

Received 7 October 2009; **Revised** 3 February 2010; **Accepted** 18 February 2010; **Published** 5 May 2010.

Seher, T., S. C. Singh, W. C. Crawford, and J. Escartín (2010), Upper crustal velocity structure beneath the central Lucky Strike Segment from seismic refraction measurements, *Geochem. Geophys. Geosyst.*, *11*, Q05001, doi:10.1029/2009GC002894.

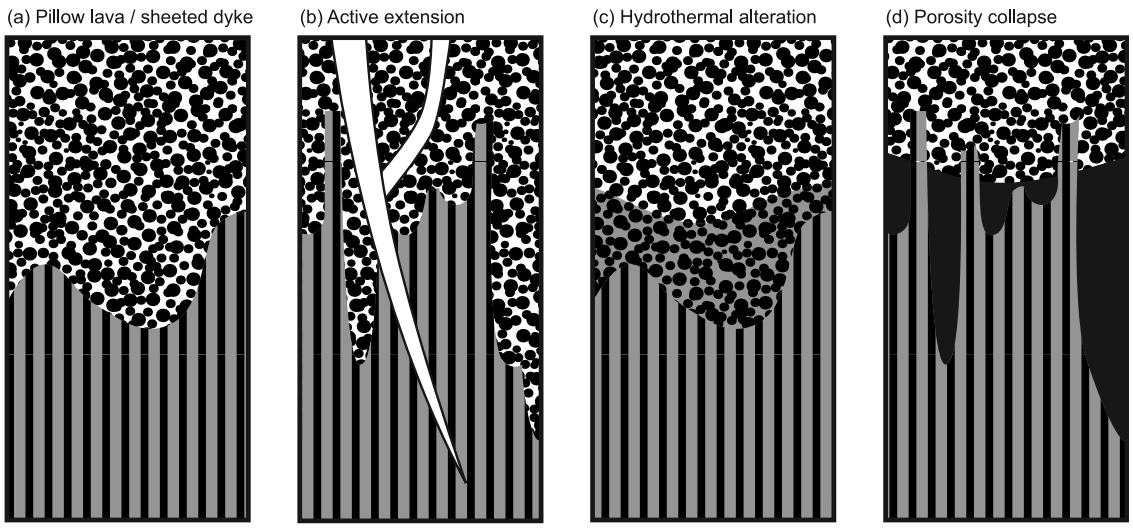

Figure 1. Illustration of different mechanisms changing the porosity structure of young upper oceanic crust. (a) Pillow lava exhibit higher porosity than the sheeted dike complex, which is linked to a porosity decrease with depth. (b) Active extension (faults, fractures, fissures, and cracks) creates additional porosity near the ridge axis. Near the surface deformation is distributed and more localized at depth, which causes a porosity decrease with depth. (c) Hydrothermal circulation can fill voids with alteration products leading to both a porosity decrease with depth and crustal age. (d) Pore space collapse caused by overburden pressure leads to a porosity decrease with depth.

1. Introduction

[2] The most popular model for young upper oceanic crust consists of an extrusive and an intrusive volcanic layer that overlie an axial magma chamber [e.g., *Karson*, 1998]. For fast spreading oceanic ridges such a model can be justified by seismic observations [*Detrick et al.*, 1987; *Toomey et al.*, 1990; *Harding et al.*, 1993; *Kent et al.*, 1993; *Christeson et al.*, 1996; *Hooft et al.*, 1996], observations of seafloor outcrops [*Francheteau et al.*, 1990; *Karson et al.*, 2002], and ophiolite studies [*Nicolas et al.*, 1988; *Nicolas and Boudier*, 1995; *Boudier et al.*, 1997]. On the contrary, at slow spreading ridges, where crustal melt lenses may be ephemeral or not exist at all [*Nisbet and Fowler*, 1978; *Sinton and Detrick*, 1992; *Smith and Cann*, 1993], upper crustal structure may not follow this simple model.

[3] Seismic studies indicate a similar velocity variation with depth for both slow and fast spreading upper crust with an upper layer of very rapidly increasing velocities and a lower layer of shallower velocity gradients, except that the upper crust is generally two times thicker at slow spreading ridges [*Hussenoeder et al.*, 2002a, 2002b]. Furthermore, upper crustal velocities increase with distance from the ridge axis in both slow and fast spreading environments [*Houtz and Ewing*, 1976; *Carlson*, 1998] and provide a temporal record of crustal development. Last, near-surface seismic velocities commonly exhibit significant azimuthal anisotropy consistent with a preferred orientation of large-scale fractures and fissures in the upper crust [*White and Whitmarsh*, 1984; *Stephen*, 1985; *Shearer and Orcutt*, 1986; *Barclay et al.*, 1998; *Dunn and Toomey*, 2001; *Tong et al.*, 2005]. Different processes have been suggested to explain these seismic observations. The dominant factor determining seismic velocities of upper oceanic crust is porosity, as pillow lava and sheeted dikes have similar composition [*Becker et al.*, 1982; *Carlson and Herrick*, 1990; *Jacobsen*, 1992]. The upper crustal porosity variations have been attributed to the following causes: (1) the pillow lava to sheeted dike boundary (Figure 1a) [*Herron*, 1982; *Harding et al.*, 1993; *Christeson et al.*, 1994; *Schouten et al.*, 1999; *Becker et al.*, 2004]; (2) active extension and deformation (Figure 1b), faults, fractures, fissures and cracks; (3) an alteration front (Figure 1c), where pores have been sealed by alteration products below a certain depth [*Rohr et al.*, 1988; *Shaw*, 1994; *Carlson*, 1998; *Grevemeyer and Bartetzko*, 2004]; and (4) a porosity threshold (Figure 1d), where pores have been closed by the overburden pressure below a certain depth [*Bratt and Purdy*, 1984; *Christeson et al.*, 2007]. These processes explain the velocity increase with depth and crustal age commonly observed near fast and slow spreading mid-ocean

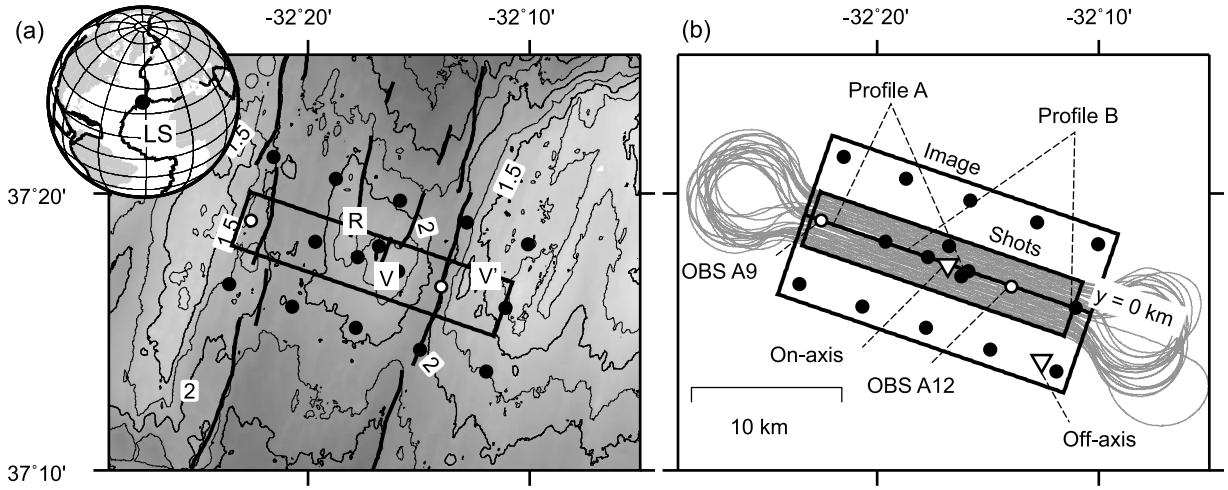

Figure 2. (a) Bathymetric map of the central part of the Lucky Strike Segment with important features of the seafloor. V, Lucky Strike volcano; R, volcanic ridge; V′, rifted volcanic edifice. The solid black lines mark the eastern and western bounding fault and a nascent fault system. Black circles mark the OBS positions, and the black box marks the shot used during the tomography study. (b) Seismic shots (grey lines) and OBS positions (circles) during the high-resolution tomography study. The outer black rectangle marks the lateral extent of the velocity model, and the inner black rectangle marks the shots. The white triangles mark the locations where on-axis and off-axis porosities are estimated and analyzed. The inset globe in Figure 2a shows the Lucky Strike Segment on the MAR. The major plate boundaries are marked as solid black lines [*Müller et al.*, 1997]. LS, Lucky Strike Segment.

ridges. However, there is no consensus about which process is dominant at different times during crustal accretion and about the role of the different processes at slow spreading ridges.

[4] To date only a few three-dimensional high-resolution tomography studies have been carried out along the Mid-Atlantic Ridge (MAR) that provide constraints on upper crustal velocity and anisotropy [*Barclay et al.*, 1998; *Dunn et al.*, 2005]. This lack of detailed seismic studies at slow spreading ridges impedes the further development of upper crustal structural models at slow spreading ridges. Our study contributes seismic constraints for upper crustal structure based on observations from the Lucky Strike Segment, where evidence for recent magmatism [*Fouquet et al.*, 1995; *Singh et al.*, 2006], widespread tectonics [*Humphris et al.*, 2002; *Escartín et al.*, 2008] and high-temperature hydrothermal circulation [*Langmuir et al.*, 1997] is found. This setting allows us to evaluate the role of the different processes in crustal creation and their development over time.

[5] We apply high-resolution seismic tomography to image the upper crust beneath the hydrothermal vents field on the Lucky Strike volcano, the surrounding median valley and the adjacent median valley walls. This wide-angle study using Ocean Bottom Seismometers (OBS) complements a concurrent 3-D seismic reflection survey. Our new results constrain the velocity structure beneath the Lucky Strike volcano to a depth of 2.5 km below seafloor (bsf) or 4.5 km below sea level (bsl). We use these results to constrain the porosity in the crust and discuss different mechanisms of upper crustal formation in the vicinity of the Lucky Strike volcano.

2. Geological Setting of the Lucky Strike Segment

[6] The Lucky Strike Segment is located at 37°N on the MAR south of the Azores triple junction between the Menez Gwen and North Famous Segments (Figure 2). The segment has a 15 km to 20 km wide median valley and a large volcano at the segment center [*Detrick et al.*, 1995; *Parson et al.*, 2000], where an axial magma chamber has been imaged seismically as a 3–4 km wide and at least 7 km long axial melt lens reflector at a depth of ~3.5 km bsf [*Singh et al.*, 2006; *Combier*, 2007] and underlying low-velocity zone extending to the crust-mantle boundary [*Seher et al.*, 2010]. Its crustal morphology is intermediate between the deep median valley of the relatively cold North Famous Segment and the pronounced axial high of the hot Menez Gwen Segment [*Thibaud et al.*, 1998].

[7] The center of the Lucky Strike Segment shows traces of recent eruptive volcanism: fresh pillow lava on the western volcanic ridge [*Ondréas et al.*, 1997] and a short-lived lava lake at the volcano summit [*Fouquet et al.*, 1995; *Humphris et al.*, 2002; *Ondréas et al.*, 2009]. The subsurface beneath the volcano and western volcanic ridge is characterized by low-resistivity anomalies [*Barker*, 2004], which may be linked to regions of elevated porosities. A regional hydrophone array recorded an earthquake swarm in 2001, which has been linked to dike injection [*Dziak et al.*, 2004]. Gravity data indicate a mantle bull's eye anomaly at the segment center, which suggests focused melt delivery and thickened crust [*Detrick et al.*, 1995; *Thibaud et al.*, 1998; *Cannat et al.*, 1999; *Escartín et al.*, 2001].

[8] There is some evidence that the Azores Hot Spot has influenced the Lucky Strike Segment [*Langmuir et al.*, 1997]. V-shaped ridges, which are normally linked to high melt supply [*Ito*, 2001], propagate south from the Azores Hot Spot [*Cannat et al.*, 1999; *Escartín et al.*, 2001]. The V-shaped ridges can today be observed as far south as the AMAR Segment (~36°40′N) [*Escartín et al.*, 2001]. Rare gas analyses shows hot spot derived melt on the MAR south of the Azores until at least ~37°N to the south of the Lucky Strike Segment [*Moreira and Allègre*, 2002]. Global seismic observations indicate melt deflection from the Azores mantle plume to the southern MAR [*Yang et al.*, 2006]. However, mantle Bouguer anomaly and bathymetric variations are relatively weak, which indicates that the Lucky Strike Segment has a lower magma supply and is in fact colder than several segments located both farther from and closer to the Azores Hot Spot [*Thibaud et al.*, 1998].

[9] Active tectonics appear to be important even during the current "magmatic" period. Axis-parallel faults are prevalent all along the seafloor [*Escartín et al.*, 2008] and there is evidence for a nascent fault system that is rifting the central volcano. Past rifting episodes are evidenced as faulted volcanic edifices.

[10] A high-temperature hydrothermal vent field sits on the summit of Lucky Strike volcano [*Langmuir et al.*, 1997]. This field has been active for hundreds to thousands of years [*Humphris et al.*, 2002]. The total heat output of the Lucky Strike hydrothermal site is of the same order as the heat output of hydrothermal sites on intermediate spreading ridges [*Jean-Baptiste et al.*, 1998]. The near-axis heat flux is consistent with fluid flow from the ridge flank toward the ridge axis [*Lucazeau et al.*, 2006] and may cause a low-magnetization anomaly underneath the Lucky Strike hydrothermal vents field [*Miranda et al.*, 2005].

3. SISMOMAR High-Resolution Tomography Experiment and Data Analysis

[11] We acquired seismic reflection and refraction data at the Lucky Strike Segment of the MAR during the 2005 SISMOMAR experiment onboard the French research vessel L'Atalante. The cruise included a 18 × 3.8 km^2 3-D multichannel seismic reflection survey while 25 OBS were deployed in an 18 × 18 km^2 box (Figure 2). The seismic source was an array of 14 air guns tuned for a sharp first break, with a total volume of 42.5 l. The air gun array was fired every 37.5 m (distance-triggered, using differential GPS) along a regular grid of lines with a line spacing of 100 m. Of the 39964 shots fired during the 3-D reflection experiment, 19539 fall along the regular grid of shot lines and were analyzed in this study (Figure 2).

[12] Only 18 of the deployed OBS were used in this study (Figure 2). The remaining seven OBS were not used because one of the OBS did not record data and the other six were located too far away to provide useful additional constraints. Eight of the 18 OBS lay inside the 3-D reflection box and ten lay less than 3 km away. Fourteen of the OBS used a 2 Hz vertical geophone and hydrophone with 2 ms sampling interval, two used a 4.5 Hz three-component geophone and hydrophone with 5 ms sampling interval, and two used a broadband three-component seismometer and a 25 ms sampling interval.

[13] The strongest arrivals registered by the OBS correspond to direct (water) waves and crustal turning waves (Pg) (Figures 3a–3d). We picked a total of 166644 arrival times (Figures 3e and 3f), which we used to construct a high-resolution subsurface velocity model from the Lucky Strike volcano and hydrothermal vents field to the median valley bounding faults. Since the instruments were located on a rugged seafloor, geophone coupling to the ground was problematic. Therefore, we used mainly the hydrophone channel for traveltime picking. Prior to traveltime estimation the two broadband sensors were band-passed between 2 Hz and 20 Hz. All other data were band-passed between 4/5 Hz and 50 Hz. After manually picking the traveltimes, we applied two corrections: (1) A static correction of 20 ms for the time delay between the trigger

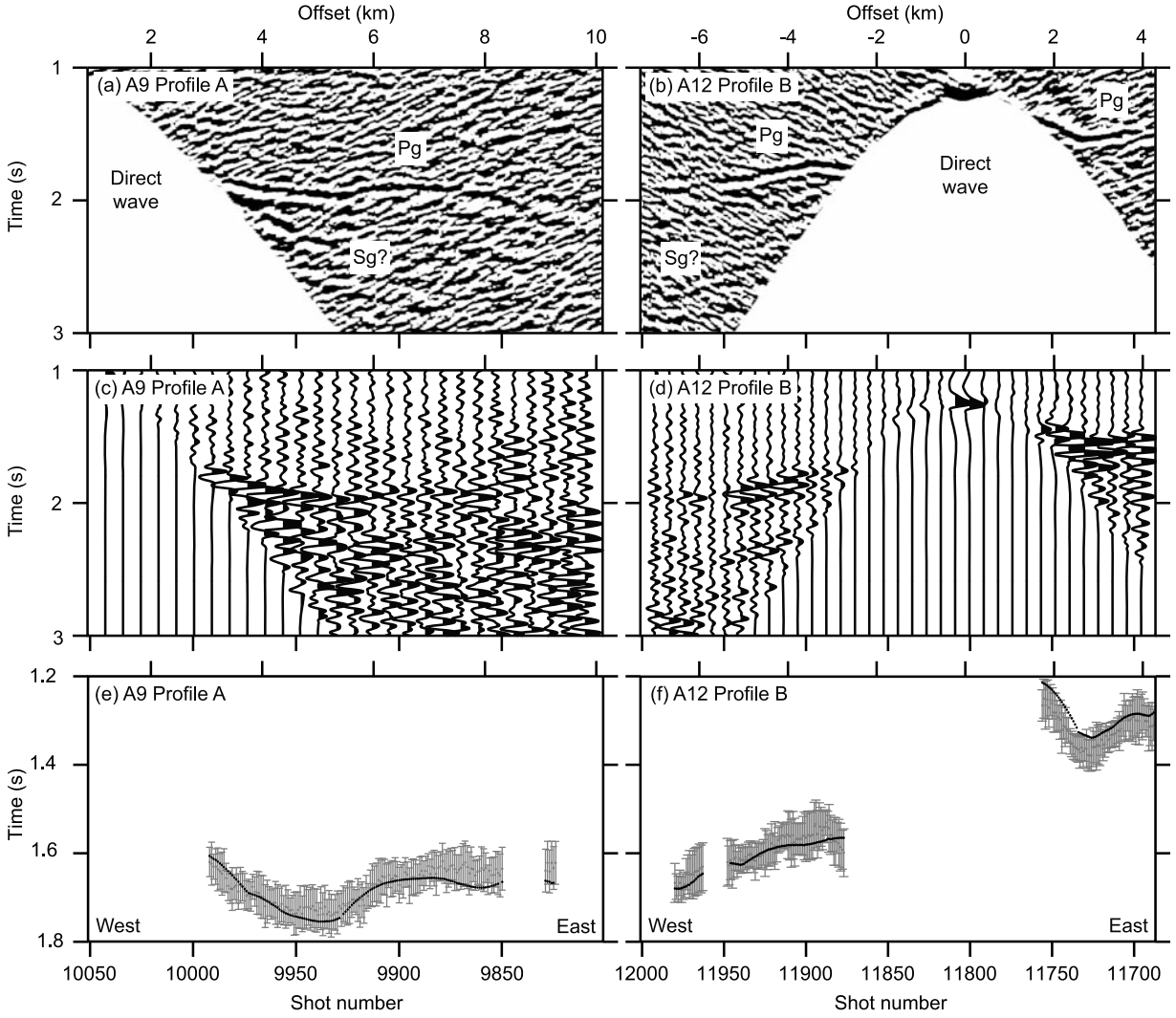

Figure 3. Example seismic data for the SISMOMAR high-resolution tomography experiment recorded at the segment center. (a, c, and e) Instrument A9 is located at the western edge of the median valley near the western bounding fault, while (b, d, and f) instrument A12 is located in the east of the volcano between the eastern median valley bounding faults and the Lucky Strike volcano (Figure 2). Record section for instrument A9 along profile A (Figure 3a) and instrument 12 along profile B (Figure 3b). Pg marks the arrival of upper crustal turning P waves, and Sg the arrival of upper crustal turning S waves. To create the record sections we applied a gain correction, a band-pass filter between 1.5 Hz and 36 Hz, a water wave mute, a predictive error filter [*Buttkus*, 2000], a linear moveout correction with a moveout velocity of 6.5 km/s, and a five-point moving average filter (trace mixing). Wiggle plots for instruments A9 (Figure 3c) and A12 (Figure 3d). To create the wiggle plots we applied an 11 trace local stack around the picked Pg arrival, a band-pass filter between 1.5 Hz and 36 Hz, and a 6.5 km/s linear moveout correction. The images in Figures 3a–3d are strongly filtered to enhance the image but were not used for traveltime picking. Traveltime picks with uncertainties and synthetic traveltimes associated with the best fitting velocity model for instruments A9 (Figure 3e) and A12 (Figure 3f) after application of a 6.5 km/s linear moveout correction. The traveltime picks and associated uncertainties (2σ) are marked as grey error bars, and the synthetic traveltimes are marked as black points.

signal and the release, and (2) a 7 ms shift of the picks to the first break on the unfiltered data.

[14] After traveltime picking, we assigned an uncertainty to every traveltime estimate. The total average traveltime uncertainty is ~30 ms and takes into account the shot location uncertainty, the receiver position uncertainty, the pick uncertainty, the uncertainties related to ray tracing, the water column velocity and the location of the seafloor. The average traveltime pick uncertainty, the uncertainty of picking a traveltime on a seismic record, amounts to ~25 ms of the total traveltime uncertainty. The

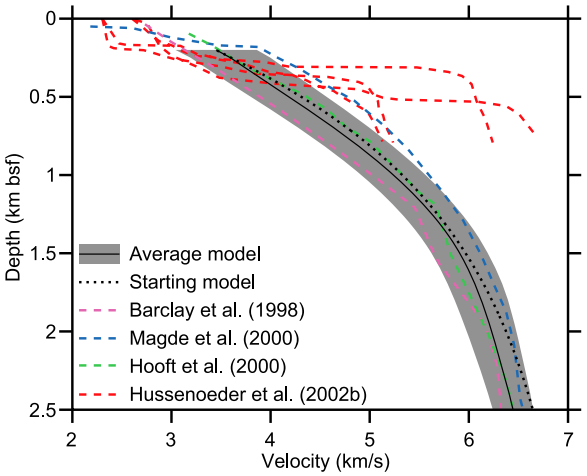

Figure 4. One-dimensional velocity-depth profiles for this study compared with profiles for the OH-1 Segment (35°N) [*Barclay et al.*, 1998; *Magde et al.*, 2000; *Hussenoeder et al.*, 2002b]. The solid black line shows the average crustal velocities for our best fitting velocity model. The grey area corresponds to one standard deviation around this average velocity model. The average crustal velocities were estimated by averaging over all well-resolved velocity nodes at the same depth below the seafloor. The standard deviation corresponds to the root mean square deviation of the velocity nodes from the average velocity model at a certain depth. The dotted black line marks the starting model used in this study. Our velocity profiles were clipped above a depth of 0.2 km bsf and below a depth of 2.5 km bsf due to insufficient resolution.

pick uncertainty is assigned based on the cross correlation between a single picked wavelet of one arrival and the mean wavelet of all the picked arrivals along one profile. A high cross correlation (>0.7) indicates a high-quality pick and is assigned a pick uncertainty of ~10 ms. A small cross correlation (<0.3) indicates a poor quality pick and is assigned a pick uncertainty of ~40 ms. For intermediate cross correlations of 0.5–0.7 and 0.3–0.5 we used a pick uncertainty of ~20 ms and ~30 ms, respectively. This method is based on the notion that the shape of the seismic wavelet does not change along one profile and can be approximated as the stack of the seismic traces. A similar method is commonly used in seismology to estimate time shifts between seismic events [*Dougherty and Stephen*, 1988; *Hung et al.*, 2004].

[15] We used the traveltime inversion method of *Hobro et al.* [2003] to constrain the velocity structure underneath the Lucky Strike volcano. In this inversion method the interfaces and subsurface velocities are described using a regular grid of nodes, which are described mathematically using B spline coefficients [*Hobro*, 1999; *de Boor*, 2001]. The velocity can be estimated at each location within the model using the evenly spaced B spline coefficients. The inversion method solves the forward problem, the calculation of synthetic traveltimes, using a ray shooting approach [*Červený*, 2001]. Ray perturbation theory is used to find a semianalytical solution to the ray equations [*Virieux and Farra*, 1991; *Chapman*, 2004].

[16] The cost function implemented in the inversion method by *Hobro et al.* [2003] contains two parts: (1) The weighted misfit between the synthetic traveltimes and the observed traveltimes, and (2) a smoothness term, that penalizes changes in model curvature [*Constable et al.*, 1987; *deGroot Hedlin and Constable*, 1990]. The relative importance of the two parameters is controlled using a regularization parameter. The inverse problem, the minimization of the cost function, is solved using the conjugate gradient algorithm [*Press et al.*, 1992]. We start the inversions with a large regularization parameter and gradually decrease the regularization with every iteration of the inversion following a jumping scheme [*Shaw and Orcutt*, 1985]. The inversion starts with both a large misfit and smoothness; both values decrease as the regularization parameter is decreased and more structure builds up in the model. The inversion is terminated once the inversion reaches a normalized misfit equal or below unity. The final model is considered satisfactory, if the ray success rate, the percentage of traveltimes observations that can be explained by tracing a ray through the velocity model, is larger than 95%. Ray tracing for a traveltime observation fails when no seismic ray arrives within 5 m from the measurement location.

[17] To start an inversion, a reasonable starting model is required. If the starting model is too far away from the true structure, the inversion does not converge. We constructed a starting model based on the average crustal velocities observed along the MAR [*Purdy and Detrick*, 1986; *Barclay et al.*, 1998; *Hooft et al.*, 2000; *Magde et al.*, 2000]. Figure 4 shows a comparison of our starting model, the average velocity distribution of our best fitting final model and velocity-depth profiles for the well-studied OH-1 Segment. Our final model stays close to our starting model. However, given a reasonable starting model (e.g., velocities increase with depth) the final model found by the inversion method is not very sensitive to the details of the starting model. The jumping scheme [*Shaw and Orcutt*, 1985] allows the velocities of the starting

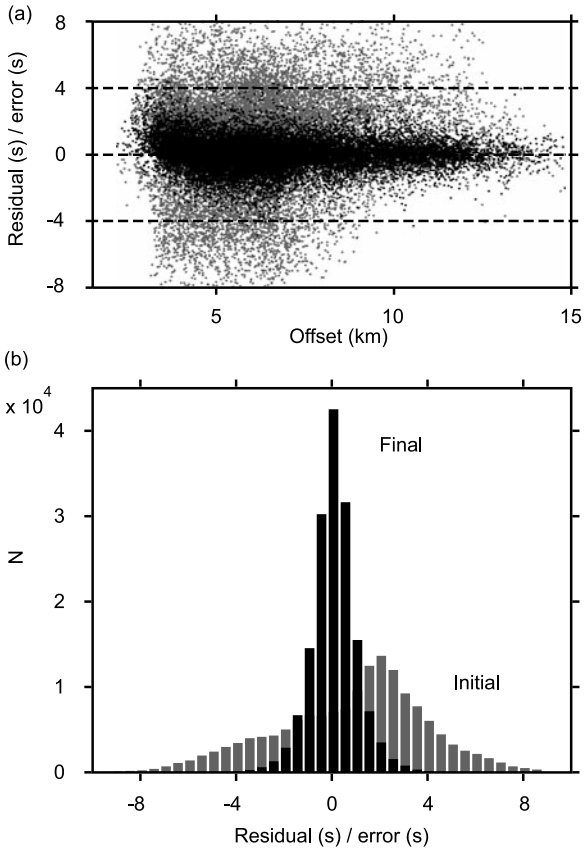

Figure 5. Comparison of normalized traveltime residuals for the starting model and the final model. (a) Variation of traveltime residuals with source-receiver offset. (b) Distribution of traveltime residuals.

models to differ significantly without causing a major change in the final solution.

[18] In this study the horizontal node spacing was 0.5 km and the vertical node spacing 0.2 km. The seafloor node spacing was 0.1 km. To avoid artifacts introduced by the rugged bathymetry, we low-pass filtered the seafloor using a Gaussian filter with a filter width of 2 km. Our preferred velocity model had a normalized misfit of $\chi^2 \approx 0.9$ and an unweighted misfit of RMS ≈ 23 ms and successfully reproduced 95% (159900/166644) of the traveltimes. Figure 5 shows the improvement of the traveltime misfit. While the initial model has a positive mean and large standard deviation, the final model shows a small standard deviation and zero mean.

4. Results

[19] Our 3-D velocity model covers the Lucky Strike volcano, the surrounding median valley and a part of the adjacent bounding walls. Here, we analyze the 3-D velocities, the velocity anomaly, and the vertical velocity gradient. The velocity anomaly is calculated by subtracting the average crustal velocity from the 3-D velocity model, after taking into account the seafloor depth. The velocity anomaly highlights deviations from a 1-D velocity distribution with respect to the seafloor. The vertical velocity gradient makes changes in the slope of the velocity model easily recognizable.

[20] Overall, seismic velocities increase rapidly in the first kilometer bsf and more gradually below (Figure 6). Interestingly, the high velocity gradient layer (>2 s^{-1}) has almost the same thickness in the median valley and underneath the valley wall, although the absolute velocities increase underneath the valley wall.

[21] At a depth of 1 km bsf, median valley velocities are at least 0.5 km/s slower than valley wall velocities (Figure 7). The low-velocity anomaly runs parallel to the ridge axis and is limited the median valley bounding faults. At a depth of 0.5 km bsf, the low-velocity anomaly is asymmetric about the Lucky Strike volcano. The low-velocity anomaly extends further to the west than to the east of the volcano, similar to the morphology of the median valley. The extent of the low-velocity zone decreases with depth. At a depth of 2 km bsf the low-velocity anomaly is symmetric about the Lucky Strike volcano. The extent of the low-velocity region (Figures 6 and 7) coincides approximately with the median valley bounding faults [*Singh et al.*, 2006; *Combier*, 2007].

[22] Recent volcanic edifices such as the Lucky Strike volcano and the northwestern volcanic ridge have the lowest velocities observed in our velocity model (Figure 7). Comparing velocities inside and outside the 2 km bsl bathymetric contour (this isobath defines approximately the limits of the Lucky Strike volcano) indicates that velocities underneath the Lucky Strike volcano are ~0.5 km/s slower than velocities underneath the surrounding median valley (Figure 7). The low-velocity anomaly underneath the Lucky Strike volcano is split into two distinct regions, the first one underlies the eastern part of the Lucky Strike volcano and the second can be found underneath the northwestern volcanic ridge.

[23] On average, the low-velocity anomalies are limited to the median valley. However, we observe an isolated velocity anomaly close to the eastern bounding wall (across-axis distance of +5 km (Figures 6b and 7)), that coincides with a topographic high to the east of OBS A12 (Figure 2). The

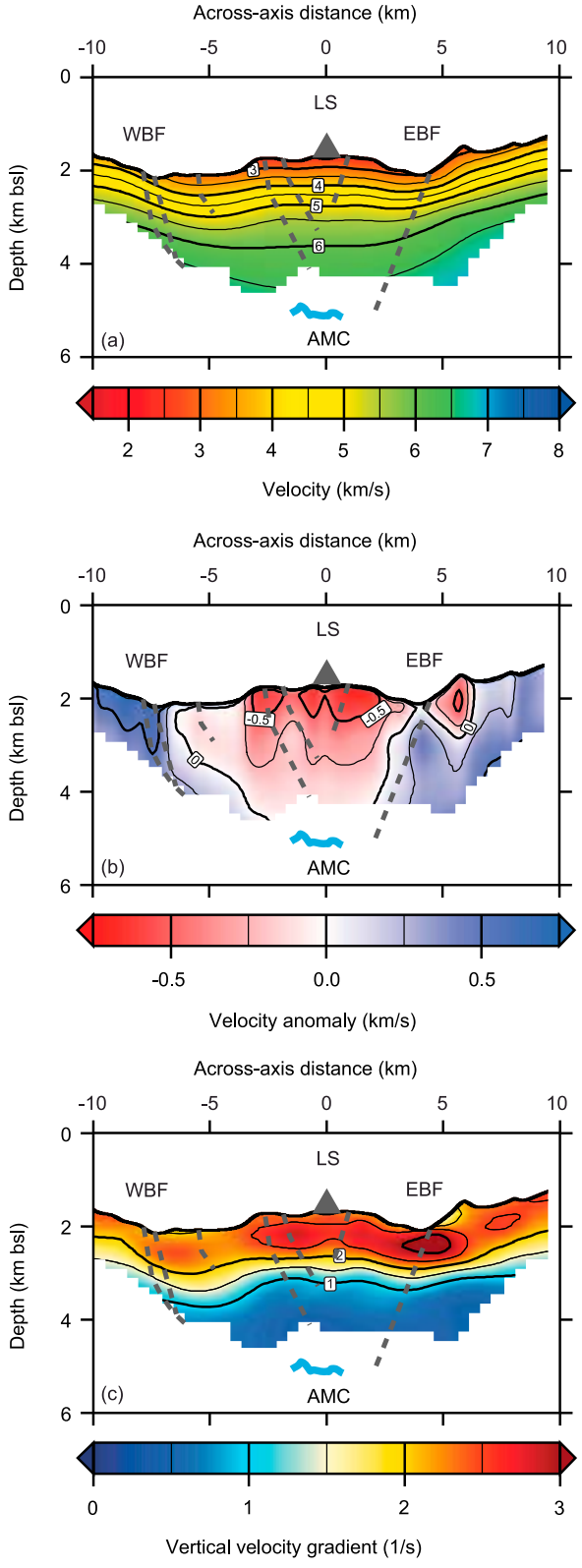

topographic high likely corresponds to part of a rifted volcano. Due to the fact that only relatively few receivers are used in the inversion, single receivers can have a large influence on the quality of the velocity model. By removing single receivers and restarting the inversion with the reduced data set we can identify regions, where the anomalies are only constrained by observations on a single instrument and may be unreliable. However, the velocity model after the removal of instrument A12 has a low-velocity anomaly underneath the eastern bounding fault.

[24] To further analyze the resolution of our velocity models we applied: (1) ray density plots [*Kissling*, 1988], (2) analysis of the posterior covariance matrix [*Tarantola*, 2005], and (3) checkerboard tests and resolvability [*Lévêque et al.*, 1993; *Zelt*, 1998, 1999].

[25] Raypaths reach a maximum depth of ~4 km bsl or ~2 km bsf along the profiles shown in Figures 8a and 8b. While the seismic rays have a large non-vertical component near the seafloor, rays at depth travel almost horizontally. The maximum turning depth of rays during this experiment is ~2.5 km bsf. The ray density [*Kissling*, 1988], the number of seismic rays crossing every grid cell, gives a rough impression of the model resolution (Figures 8c and 8d). Velocity values in grid cells without ray coverage cannot be constrained. However, a high ray density does not necessarily indicate that a model cell is well resolved, because seismic waves that take the same path through the subsurface do not contribute to the resolution.

[26] Analysis of the diagonal terms of the posterior covariance matrix [*Tarantola*, 2005] allows an assessment of the model parameter uncertainty. The final model uncertainties for our favorite velocity are shown in Figures 8e and 8f and correspond to one standard deviation. The model uncertainty resembles to the ray density; areas of high ray density are

Figure 6. Vertical slice through the best fitting velocity model at an along-axis distance of 0 km, i.e., directly through the segment center. The grey triangle marks the position of the Lucky Strike volcano (LS), the dashed grey lines mark the positions of the major faults (WBF and EBF, western and eastern bounding faults, respectively), and the cyan line marks the location of the axial melt lens reflector (AMC) [*Combier*, 2007]. Velocity nodes with no ray coverage have been masked. The vertical exaggeration is 2:1. (a) Velocity distribution. (b) Velocity anomaly estimated by subtracting the velocity from the average crustal velocity structure (Figure 4). (c) Vertical velocity gradient.

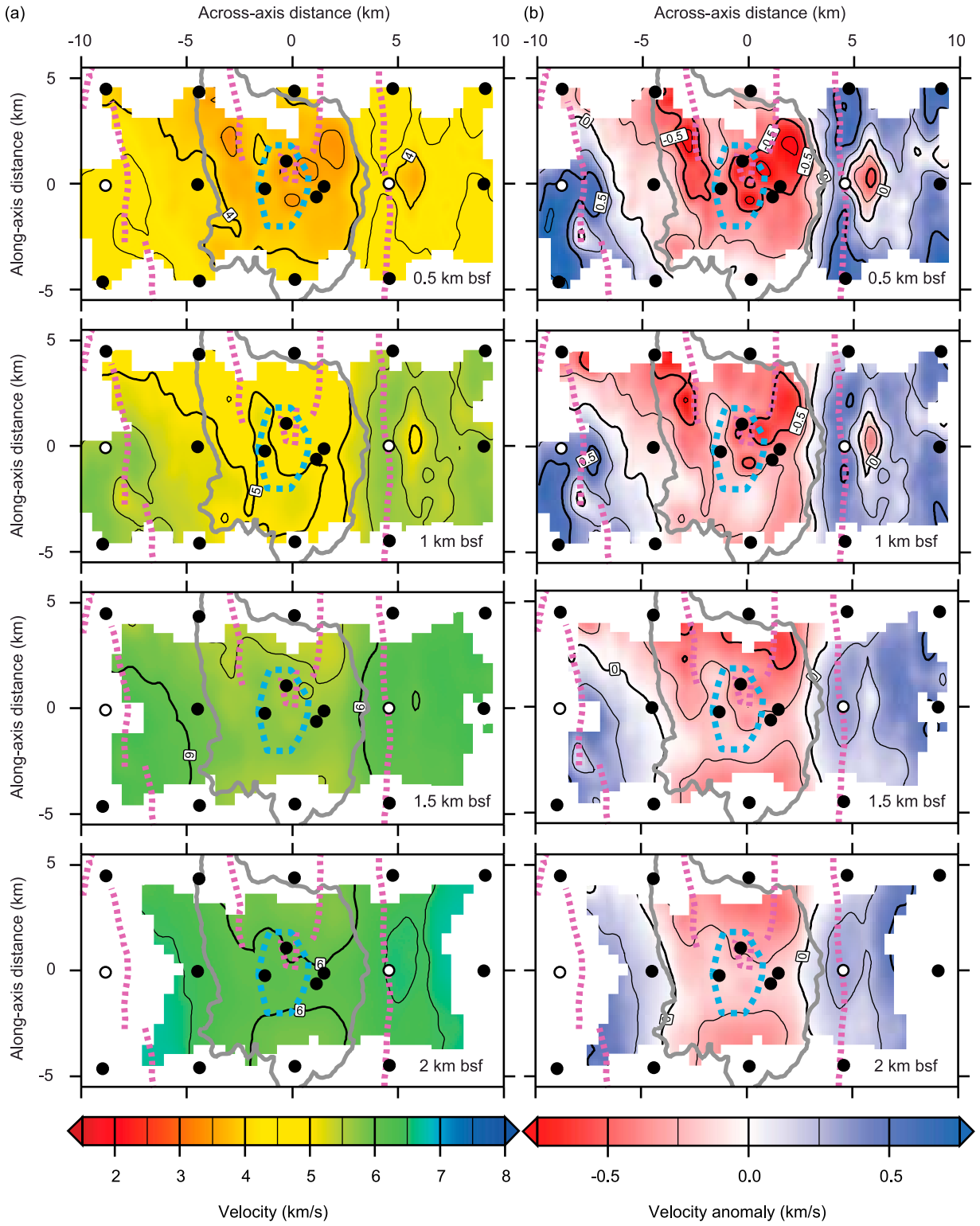

Figure 7. Upper crustal velocity structure at a depth of 0.5, 1, 1.5, and 2 km bsf. The black circles mark the OBS locations. The white circles highlight the locations of OBS A9 in the west and OBS A12 in the east. The dashed magenta lines mark the positions of the eastern and western bounding faults and of a nascent fault system on top of the volcano. The outline of the volcano, 2 km depth bsl, is marked as a solid grey line. The outline of the axial melt lens reflector [*Combier*, 2007] is marked using a dashed cyan line. (a) Velocity. (b) Velocity anomaly.

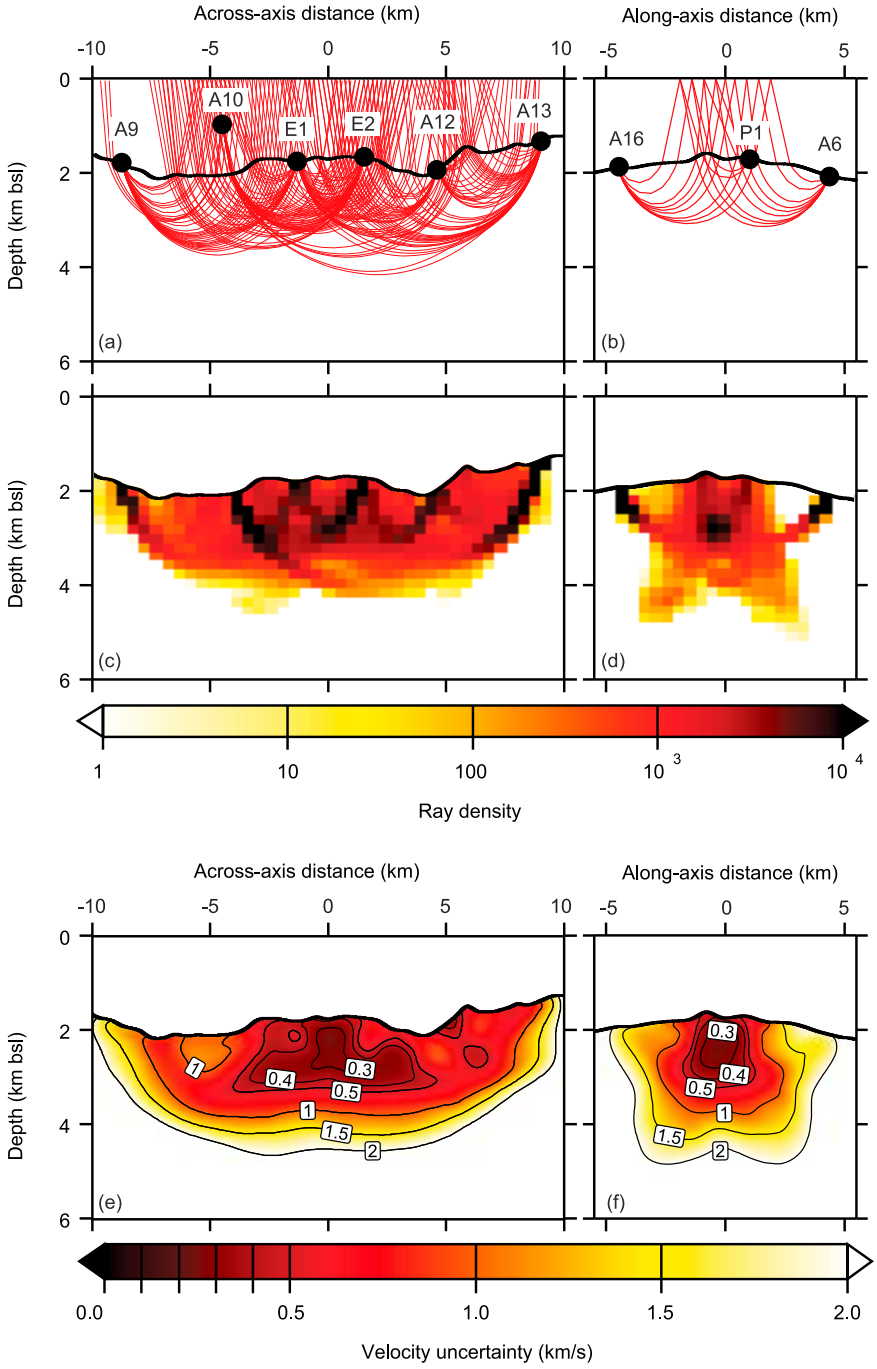

Figure 8. Resolution analysis for the best fitting velocity model. (a) Raypaths for six OBS located along a single shot line across the volcano. The number of rays was reduced by a factor 10. OBS A10 was anchored 1 km above the seafloor. (b) Raypaths for three OBS located around across-axis distance 0 km for a single shot on all 39 profiles. The number of rays was reduced by a factor 5. (c and d) Logarithmic ray density showing the number of rays crossing each grid cell. (e and f) Velocity uncertainty. The vertical exaggeration is 2:1.

characterized by a low-velocity uncertainty. These uncertainties are valid for small perturbations around the final model only [*Hobro et al.*, 2003].

[27] Checkerboard tests [*Lévêque et al.*, 1993; *Zelt*, 1998, 1999] are a systematic approach for analyzing the resolvability of velocity anomalies with certain wavelength characteristics. Our velocity model shows stronger vertical than horizontal velocity variations. Therefore, the horizontal wavelength λ_h for the checkerboard tests was chosen to be approximately 2.5 times larger than the vertical

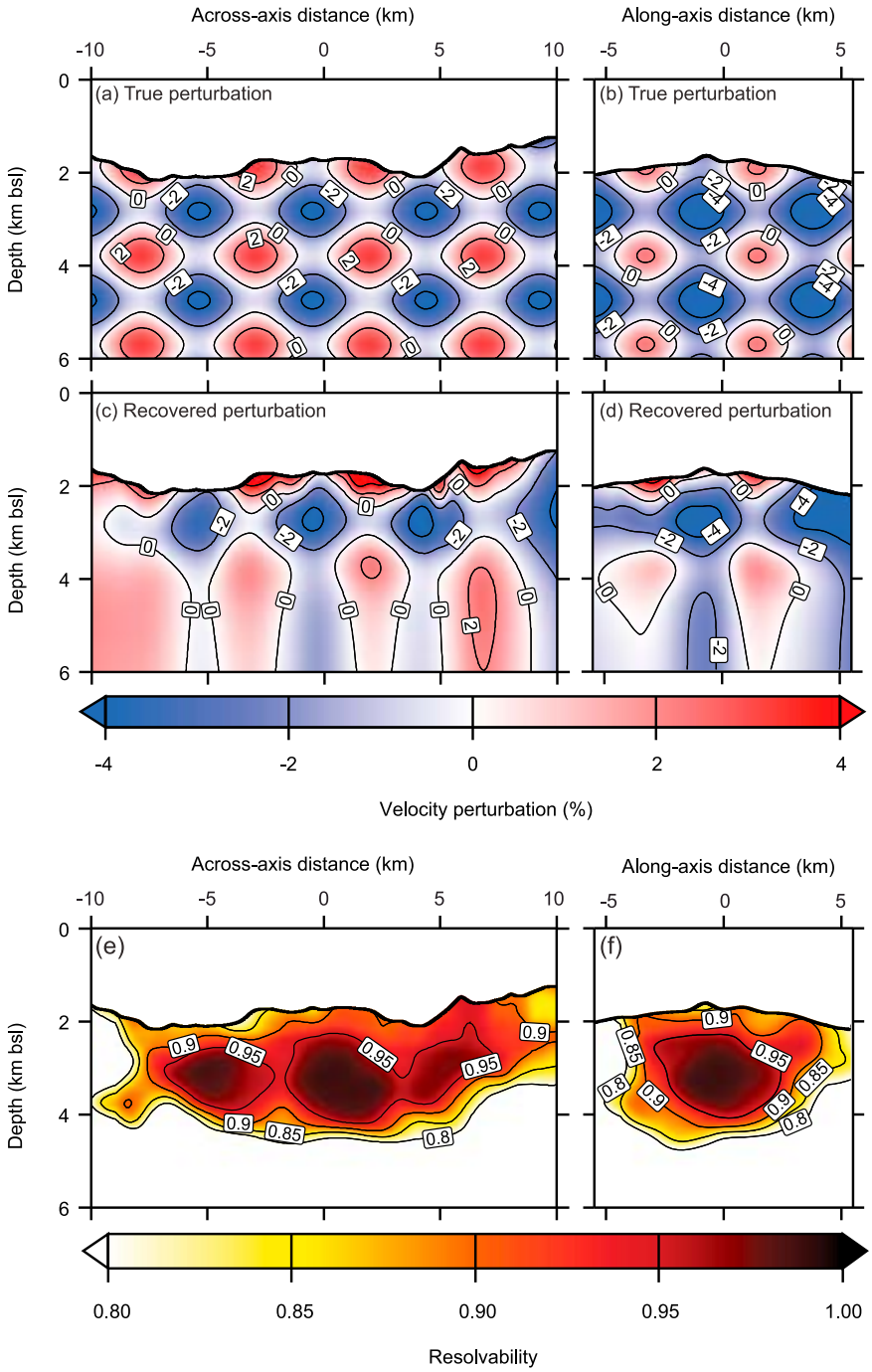

Figure 9. Example of checkerboard test performed for pattern 2 ($\lambda_h \approx 4.8$ km and $\lambda_v \approx 1.9$ km). (a and b) Perturbation added to best fitting velocity model and used in the forward calculation. (c and d) Perturbation recovered by the inversion. (e and f) Resolvability or averaged semblance between true and recovered perturbations using four different checkerboard patterns with the same spatial wavelengths as the one shown in Figures 9a and 9b. The slices shown here run perpendicular and parallel to the ridge axis across the volcano. The vertical exaggeration is 2:1.

wavelength λ_v. We analyzed three different perturbations patterns. Checkerboard pattern 1 ($\lambda_h \approx$ 2.9 km, $\lambda_v \approx 1.2$ km) corresponds to approximately six times the node spacing, pattern 2 ($\lambda_h \approx 4.8$ km, $\lambda_v \approx 1.9$ km) to approximately ten times the node spacing, and pattern 3 ($\lambda_h \approx 6.8$ km, $\lambda_v \approx 2.7$ km) to approximately fourteen times the node spacing of the velocity model. To perform a checkerboard test, a sinusoidal anomaly pattern is added to the best fitting velocity model. This velocity model is used

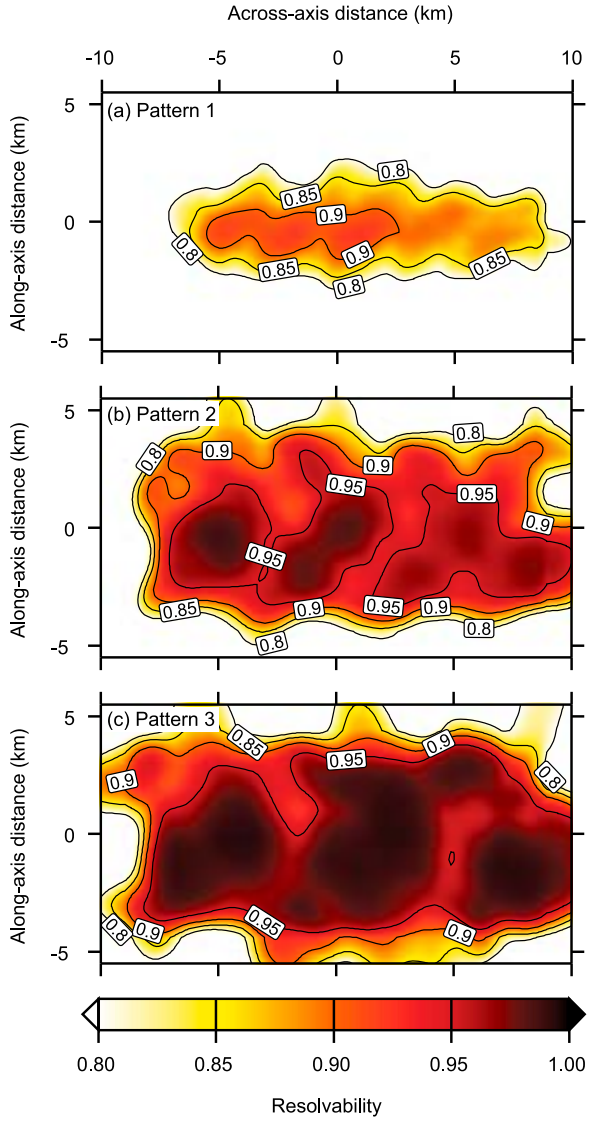

Figure 10. Resolvability or averaged semblance for checkerboard patterns (a) 1 ($\lambda_h \approx 2.9$ km and $\lambda_v \approx 1.2$ km), (b) 2 ($\lambda_h \approx 4.8$ km and $\lambda_v \approx 1.9$ km), and (c) 3 ($\lambda_h \approx 6.8$ km and $\lambda_v \approx 2.7$ km). The slices shown here are located at a constant depth of 1 km below the seafloor. The resolvability shown in Figure 10b corresponds to the resolvability shown in Figures 9e and 9f.

in the forward calculation and later compared with the velocity model recovered by the inversion. Where the model is well constrained, each positive and negative anomaly in the forward model should match an anomaly in the inverse model (Figures 9a–9d). The same procedure was repeated four times with a checkerboard pattern shifted by a quarter wavelength. Last, the semblance between the velocity anomaly used in the forward calculation (Figures 9a and 9b) and the recovered velocity anomaly (Figures 9c and 9d) is estimated and averaged for four checkerboard patterns yielding the averaged semblance or resolvability (Figures 9e and 9f). Comparing the resolvability (Figures 9e and 9f) with the ray density (Figures 8c and 8d) shows that a cutoff between a resolvability of 0.7 and 0.8 is appropriate. Velocity cells with a semblance below 0.7 or 0.8 commonly have a ray density of zero and are not constrained by any seismic rays. *Zelt* [1998] suggests a limit of 0.7.

[28] The resolvability of velocity anomalies increases with wavelength (Figure 10). Recovering the short-wavelength anomaly pattern 1 (Figure 10a) is more difficult than recovering the long-wavelength anomaly pattern 3 (Figure 10c). All three checkerboard patterns cannot be recovered close to the seafloor due to the geometry of the raypaths; that is, most rays travel almost vertically.

[29] The different resolution tests demonstrate that both the long-wavelength velocity increase with distance from the ridge axis and the short-wavelength low-velocity anomalies underneath the Lucky Strike volcano and eastern bounding wall are required by our observations. However, all three methods (ray density, resolvability and posterior covariance matrix) have limitations. Ray density is insensitive to the geometry and limited angular coverage of an experiment. The averaged semblance tends to overestimate the resolution both laterally and vertically due to the influence of smoothing on the inversion. The semblance may indicate a significant resolvability (>0.7–0.8) in the absence of any crossing rays. Estimation of the posterior covariance matrix ignores the nonlinearity of the inverse problem, the possible correlation between model parameters and depends on the shape of the cost function at convergence. While checkerboard tests examine anomalies larger than one grid cell, analysis of the posterior covariance matrix treats each model cell separately. This explains, why the resolvability shows that velocity perturbations smaller than 4% can be recovered in well-constrained region of the velocity model, while the diagonal terms of the posterior covariance matrix indicate that the velocity uncertainty in this part of the model may be larger than 10%.

[30] The most important test of model quality is, whether the velocity model reproduces the observed traveltimes to within the observed uncertainties. Our velocity model permits us to fit the observed traveltimes to within a root mean square misfit of 23 ms and overall the traveltime residuals follow a Gaussian distribution with a zero mean. How-

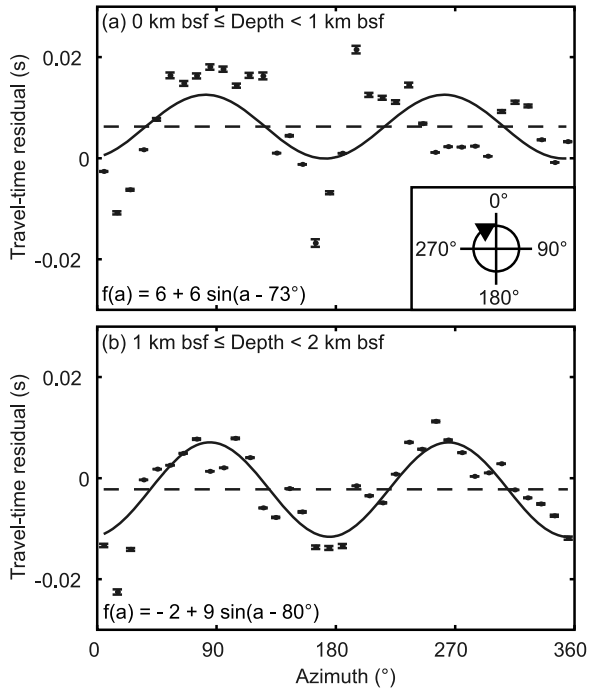

Figure 11. Average traveltime residual for all instruments. The traveltime residuals were averaged (a) between 0 and 1 km bsf and (b) between 1 and 2 km bsf. Below 2 km bsf insufficient azimuthal coverage does not allow to estimate a reliable mean traveltime residual. The formula gives the best fitting sinusoid. The error bars show the uncertainty of the mean residuals. The inset to Figure 11a illustrates the azimuths. 0° is parallel to the ridge axis (≈19°N.)

ever, we observe a systematic variation with both offset and azimuth, but those variations (<10 ms) are significantly smaller than the mean traveltime uncertainty.

[31] The variation of traveltime residuals with offset shows that at small offsets the calculated traveltimes are systematically smaller than the observed traveltimes (Figure 5) implying that the near-surface velocity model is too fast for those observations. There are two possible explanations for this effect: (1) The inversion method underestimates the velocity gradient at shallow depth due to the smoothness regularization or (2) there is a significant difference between horizontal and vertical velocity, i.e., anisotropy. In scenario 1 the inversion method overestimates poorly constrained velocities at shallow depths, because the smoothness regularization effectively minimizes the vertical curvature of the velocity model. This causes the small velocity gradient in the well-constrained lower part of the model to be extrapolated to shallow depths, where a higher velocity gradient would be required. In scenario 2 vertical velocities are faster than horizontal velocities. In the near surface, most raypaths are almost vertical and preferentially sample vertical velocities. However, the near-offset observations have a significant nonvertical component, but very little influence on the inversion compared to the large number of far-offset observations.

[32] Prior studies of the MAR have shown evidence for anisotropic upper crustal velocities that cause a sinusoidal variation of traveltime residuals with azimuth [*Barclay et al.*, 1998; *Dunn et al.*, 2005; *Seher et al.*, 2010]. To assess whether an azimuthal velocity variation is present in our velocity models, we average the traveltime residuals (the observed traveltimes minus the calculated traveltimes) with respect to source-receiver azimuth in 10° wide bins. We then fit a sinusoid to the binned traveltime residuals, which allows us to estimate an azimuth-independent residual as well as amplitude and phase of the sinusoidal variation (Figure 11). A more rigorous treatment is given by *Backus* [1965]. We observe an azimuthal variation of traveltime residuals consistent with an isotropic velocity model being used for an anisotropic velocity distribution. The amplitude of the sinusoid is 6 ms for rays with turning depths smaller than 1 km bsf and 9 ms for rays with turning depths between 1 and 2 km bsf. Rays traveling parallel to the ridge axis show negative residuals and rays traveling orthogonal to the ridge axis positive residuals. This implies that the velocity model is too slow for rays traveling along the ridge axis and too fast for rays traveling across the ridge axis. The phase of the sinusoid is 73° for turning depth of 0–1 km and 80° for turning depth of 1–2 km. The fast direction is oriented ~0–5°N, which is ~10–15° toward the North away from the ridge axis.

5. Porosity Estimate

[33] The velocity structure of young upper oceanic crust (seismic layer 2) is mainly determined by differences in porosity, which typically varies between 0% and 20% [*Becker et al.*, 1982; *Becker*, 1985]. By mapping velocity variations to porosity variations we ignore the influence of (1) temperature, (2) pressure, and (3) variable pore geometry.

[34] 1. Pillow lava are cooler than the sheeted dikes and should therefore have higher matrix velocities. However, the reverse is observed and velocities in the lower crust are larger than near the surface.

[35] 2. The presence of porosity leads to a pressure dependence of upper crustal velocities, which is primarily linked to the closure of pore spaces and not the compaction of the rock matrix itself. The pressure in the crust is determined by two factors, the pressure of the water column and the pressure of the rock matrix. Typical water depths are 1–2.5 km bsl and the depth range of interest is 0–2 km bsf. Applying a simple velocity-confining pressure relationship [*Christensen*, 1984; *Wepfer and Christensen*, 1991] shows that changing the water depth by 1.5 km leads to a velocity change of 0.1 to 0.2 km/s. Similarly, moving from 0 to 2 km bsf yields a velocity change of ~0.3 km/s. These velocity variations are significantly smaller than the variations observed in our velocity models.

[36] 3. We assume that the nature of the porosity remains the same down section and ignore possible changes in pore geometry caused by a transition from pillows/flows/sills to dikes.

[37] Any other process such as weathering or alteration would effect porosity. Weathering would likely decrease the overall velocity of basalt, but this change would be small compared with other causes for porosity reduction (pore space collapse or alteration). Furthermore, the observed velocity increase off axis is inconsistent with weathering, since older crust would have experienced more weathering and should therefore have lower velocities. Alteration by hydrothermal circulation is likely heterogeneous and associated with hydrothermal recharge and discharge systems (e.g., Lucky Strike hydrothermal field). Alteration would weaken the rock and promote pore space collapse and infill. This process is probably secondary to porosity collapse, particularly when we know that lava emplacement results in large amounts of porosity.

[38] Porosity-velocity relationships for a mixture of basalt and water can be described using theoretical bounds and deterministic models. However, the theoretical upper and lower Hashin-Shtrikman bounds for two-phase materials [*Hashin and Shtrikman*, 1963] do not narrow the range of porosities because of the large contrast in physical parameters between water and basalt [*Nur et al.*, 1998]. We will therefore model the porosities required to explain the observed velocities using effective medium theory (EMT). There are two classes of EMT, the differential effective medium theory (DEM) and self-consistent effective medium theory (SC). DEM describes a composite material by introducing infinitesimal changes into an already existing composite [*Norris*, 1985; *Berryman et al.*, 2002]. SC on the other has no host material and all components are treated equal [*Budiansky*, 1965; *Hill*, 1965]. While SC gives accurate estimates for granular media such as sandstones, DEM gives better results for rocks having isolated cracks like basalt [*Berge et al.*, 1993]. Recent geophysical EMT applications include the modeling of the elastic properties of shales [*Hornby et al.*, 1994], hydrate-bearing sediments [*Jakobsen et al.*, 2000] and axial magma chambers at mid-ocean ridges [*Mainprice*, 1997; *Taylor and Singh*, 2002].

[39] EMT allows the prediction of seismic velocities assuming a porosity ϕ and a given crack geometry with the inverse aspect ratio r = c/a. Here, c and a denote the polar and equatorial radius, respectively. For spherical inclusions (r = 1) and random elliptical inclusions (r > 1) estimated velocities are isotropic. For aligned elliptical inclusions (r > 1) velocities become anisotropic and we observe slower velocities parallel to the equatorial axis of the ellipsoidal inclusion and faster velocities parallel to the polar axis [*Taylor and Singh*, 2002]. To compare the estimated anisotropic velocities to velocities in our velocity model, we assume that the slow direction is oriented horizontally and the fast direction vertically. This choice is motivated by the observation of axis-parallel faults (Figure 2) [*Escartín et al.*, 2008; *Ondréas et al.*, 2009]. There is a trade-off between the inverse aspect ratio and the degree of alignment of the cracks; for a given inverse aspect ratio r fully aligned cracks produce the slowest velocities. Introducing random cracks increases the seismic velocities. For a given inverse aspect ratio, our estimated porosities will therefore be minimum values.

[40] In our modeling we assume a two-phase effective medium made up of basalt ($V_p \approx 6.4$ km/s, $V_s \approx 3.5$ km/s, $\rho \approx 2971$ kg/m^3 [*Johnston and Christensen*, 1997]) and seawater ($V_p \approx 1.5$ km/s measured during the SISMOMAR cruise, $V_s = 0$ km/s, $\rho \approx 1030$ kg/m^3 [*Telford et al.*, 1990]). The basalt values are based on measurements on rocks recovered from boreholes at zero porosity ($\phi = 0\%$) and a pressure of 200 MPa [*Johnston and Christensen*, 1997]. We assume these values to be close to values for unfractured basalt. The inverse pore aspect ratio determined using the approach by *Cheng and Toksöz* [1979] typically varies between 1 and 2000 for basalt [*Johnston et al.*, 1995]. The largest part of the porosity is shown to be accommodated by pores with an inverse aspect ratio between 10 and 1, but the inverse aspect ratio is poorly constrained [*Johnston and Christensen*, 1997]. Starting with a solid basalt with $\phi = 0\%$, we gradually increase the

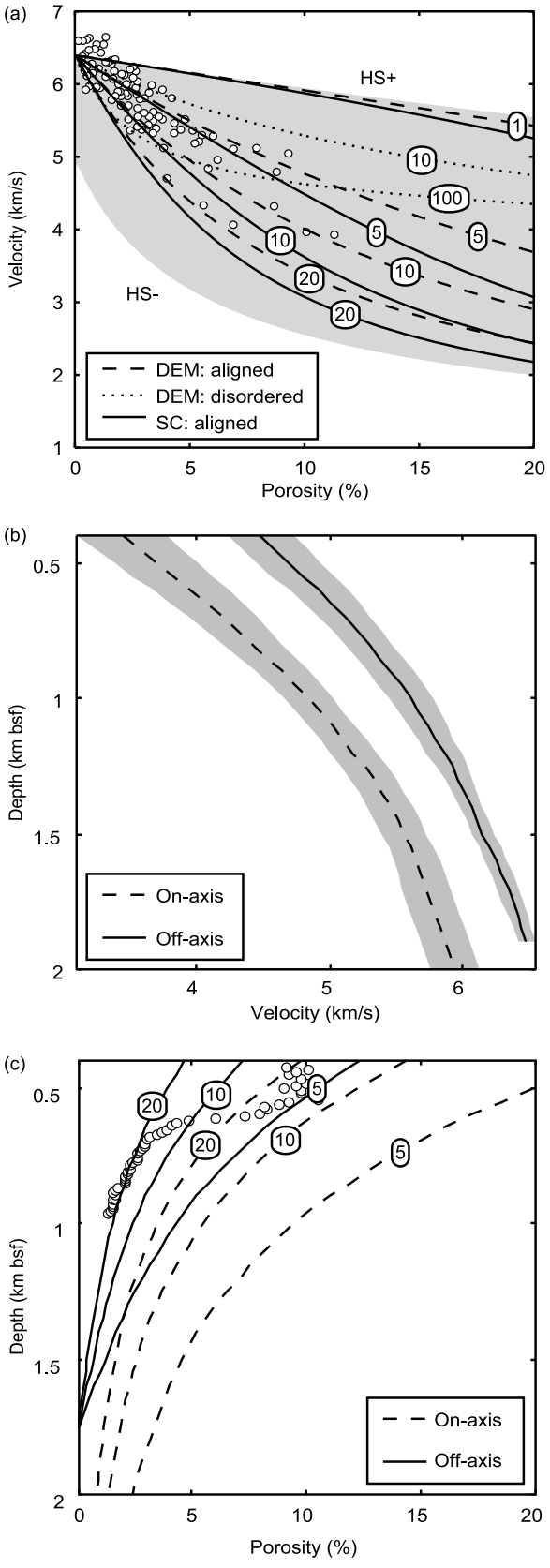

porosity to the critical porosity ϕ = 20% [*Nur et al.*, 1998], where the rock would pass from frame supported to fluid supported.

[41] We apply EMT to analyze three features of our velocity models, the velocity increase with depth, the off-axis velocity increase and last the azimuthal distribution of traveltime residuals. First, we test the EMT predictions using laboratory measurements [*Johnston and Christensen*, 1997] (Figure 12a). While assuming spherical inclusions (r = 1) the EMT predictions do not fit the laboratory data. Fully aligned elliptical inclusions (r = 5,10,20) and disordered elliptical inclusions (r = 10,100) can explain the laboratory data. However, the range of velocities present in our models (Figure 12b) requires the presence of fully aligned inclusions.

[42] Explaining the velocity increase with depth requires cracks with an inverse aspect ratio of ~5–20 and a porosity decrease with depth of 6%–17% on axis and 4%–11% off axis (Figure 12c). Explaining the velocity increase with distance from the ridge axis requires a porosity decrease of 4%–9% at 0.5 km bsf and 1%–3% at 1.75 km bsf (Figure 12c). In our model porosities have been sealed off axis at a depth of 1.75 km bsf. However, porosities could be nonzero, if a higher velocity were chosen for unfractured basalt. The magnitude of our porosities estimates agrees well with the

Figure 12. (a) Estimation of subsurface porosity. White circles show subset of laboratory measurements [*Johnston and Christensen*, 1997]. The grey area in the background shows the upper and lower Hashin-Shtrikman bounds (HS− and HS+) for two-phase materials. The solid and dashed lines mark velocity estimates using self-consistent (SC) and differential effective medium theory (DEM). For SC cracks are aligned, while for DEM both aligned and randomly oriented crack distributions were used. The number denotes the inverse of the aspect ratio (the quotient of polar and equatorial radius) [*Taylor and Singh*, 2002]. A value of 1 denotes spherical inclusions, and a value larger than 1 corresponds to prolate inclusions. For elliptical aligned inclusions the velocity in the slow direction is shown. (b) Vertical velocity profiles at on-axis and off-axis reference locations (Figure 2). The values were obtained by averaging in an 2 × 2 km^2 area. The grey area corresponds to twice the standard deviation for the averaged depth interval. (c) Subsurface porosity distribution estimated using aligned DEM. The dashed and sold lines mark the porosities on and off axis. The numbers give the inverse aspect ratio. The data show apparent bulk porosities for ODP Hole 504B [*Becker et al.*, 1982; *Becker*, 1985, 1990] for comparison.

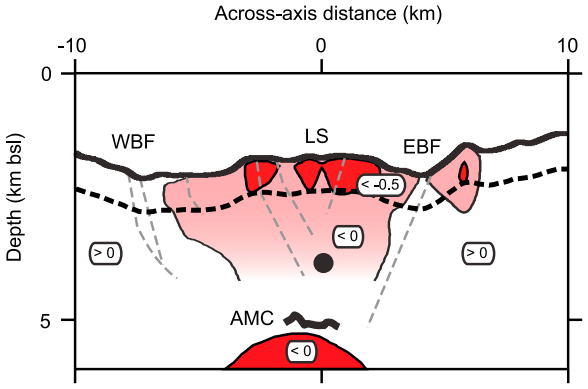

Figure 13. Sketch integrating results from different seismic studies of the Lucky Strike Segment. The location of the faults (dashed grey lines) and axial melt lens reflector (AMC) is based on the seismic reflection study by *Combier* [2007]. The location of the segment center low-velocity anomaly beneath the axial melt lens reflector is based on the seismic tomography studies by *Seher et al.* [2010]. The location of the layer 2A event (dashed black line) is based on the study by Seher et al. (submitted manuscript, 2010). The location of the upper crustal low-velocity anomalies were derived in this study. The black circle marks an upper crustal microseismic event observed by *Dusunur et al.* [2009]. LS, Lucky Strike volcano and hydrothermal system; WBF and EBF, western and eastern bounding faults, respectively. The vertical exaggeration is 2.

porosities measured in Hole 504B [*Becker et al.*, 1982; *Becker*, 1990].

[43] Lastly, we observed a sinusoidal variation of traveltime residuals with azimuth with an amplitude of 6–9 ms (Figure 11). To link the observed traveltime residuals to anisotropy, we estimate synthetic traveltimes for a constant velocity gradient model, that best fits our mean velocity model to the approximate turning depth within each depth interval. The observed peak-to-peak variation requires a velocity anisotropy of ~1.5%. This compares well to the velocity anisotropy of 2%–4% observed in the OH-1 Segment using a tomography method including velocity anisotropy [*Barclay et al.*, 1998; *Dunn et al.*, 2005].

[44] This anisotropy can be explained by EMT using an inverse aspect ratio r = b/a, where b and a stand for the crack radius in along- and across-axis direction, respectively. This azimuthal anisotropy is consistent with aligned cracks that are compressed in across-axis direction and elongated in along-axis direction. At a porosity of 12% typical for a depth of 0.5 km bsf, an inverse aspect ratio of 1.1 creates 3% velocity anisotropy, while at a porosity of 3% typical for a depth of 1.5 km bsf an inverse aspect ratio of 1.3 is necessary to explain a similar velocity anisotropy. In conclusion, aligned cracks that are 10%–30% more elongated along the ridge axis than across the ridge axis are sufficient to explain the observed azimuthal anisotropy.

6. Discussion

[45] Our high-resolution 3-D tomography study contributes to our knowledge of the upper crustal seismic structure in the Lucky Strike Segment (Figure 13). The upper crust underneath the Lucky Strike volcano and the western volcanic ridge shows pronounced low-velocity anomalies. Similar low velocities were observed beneath an axial seamount at 35°N on the MAR [*Barclay et al.*, 1998].

[46] Magmatic processes have a significant influence on the upper crustal structure in the central Lucky Strike Segment. Younger pillow lava are commonly characterized by lower velocities because of their higher porosity, since both tectonic and hydrothermal processes have not yet significantly decreased crustal porosities. A link between younger crust and low velocities explains why the lowest velocities are found underneath recent volcanic edifices (e.g., the Lucky Strike volcano and the western volcanic ridge). These edifices contain large amounts of relatively fresh pillow lava [*Humphris et al.*, 2002; *Escartín et al.*, 2008; *Ondréas et al.*, 2009], which would create higher porosities and thereby lower velocities. Furthermore, the low-velocity anomalies are located above the seismic layer 2A-2B boundary (T. Seher et al., Seismic layer 2A variations in the Lucky Strike segment at the Mid-Atlantic Ridge from reflection measurements, submitted to *Journal of Geophysical Research*, 2010) (Figure 13), which is commonly identified with the lava to sheeted dike transition [*Herron*, 1982; *Harding et al.*, 1993]. While layer 2A velocities are poorly resolved, systematic resolution analysis has shown that the velocity model is reliable at least in the lower part of seismic layer 2A. We, therefore identify the upper crustal low-velocity anomalies with recently erupted pillow lava.

[47] The local low-velocity anomalies are located above the seismic layer 2A-2B boundary. While a coincident segment-scale seismic reflection study (Seher et al., submitted manuscript, 2010) has shown that the layer 2A-2B event does not require large-scale variations in layer 2A thickness, a high-resolution reflection study of the Lucky Strike

volcano indicates that such layer 2A thickness variations may exist [*Combier*, 2007]. Our study does not allow any conclusion about the nature of the seismic layer 2A-2B boundary, since layer 2A velocities are only poorly constrained by OBS tomography studies (this may also explain the uniform upper crustal velocity gradient). Any abrupt change at the layer 2A–2B boundary would appear smooth in our velocity models. However, the observed velocities allow inferences about upper crustal porosities. The pillow lava to sheeted dike transition is commonly linked to a large porosity contrast [*Herron*, 1982; *Harding et al.*, 1993]. If the pillow lava to sheeted dike transition occurs over a large depth range [*Barclay et al.*, 1998], a lithologic boundary explains the gradual increase of upper crustal velocities with depth. Alternatively, a porosity threshold may create a depth below which pores have been closed by the overburden pressure [*Bratt and Purdy*, 1984; *Christeson et al.*, 2007], which would explain the velocity increase with depth. Last, an alteration front can create a depth below which pores have been sealed by alteration products [*Rohr et al.*, 1988; *Christeson et al.*, 2007].

[48] The local low-velocity anomalies underneath the Lucky Strike volcano are embedded in a zone of decreased velocities that spans the entire median valley and is limited on both sided by the eastern and western median valley bounding faults. The low-velocity anomaly inside the median valley is similar to that observed at 35°N [*Magde et al.*, 2000]. The low-velocity zone narrows toward the axial magma chamber characterized by a lower crustal low-velocity zone [*Seher et al.*, 2010] and axial melt lens reflection [*Singh et al.*, 2006; *Combier*, 2007]. Interestingly, we observe an asymmetry of the zone of decreased velocities with respect to the Lucky Strike Volcano that disappears with depth. While this asymmetry could be caused by the loss of resolution with depth, it may be linked to the geometry of the median valley bounding faults. Magmatic accretion is likely limited by the median valley bounding faults and the zone of decreased velocity underneath the median valley may be linked to volcanic accretion limited by the faults. The asymmetry may be caused by a thicker lava layer underneath the Lucky Strike volcano. Alternatively, the median valley bounding faults may limit a zone of active extension (faults, fractures, fissures) and widespread normal faulting, that causes the creation of additional pore spaces. Last, the tectonic deformation may be distributed in the near surface and focused along major faults at depth, which explains the asymmetry as well as the velocity increase and associated porosity decrease with depth.

[49] We observe a rapid velocity increase coincident with median valley walls. Velocities underneath the valley walls at a distance of 8 km from the ridge axis (~0.7 Ma) are ~1 km/s faster than underneath the Lucky Strike volcano. A similar velocity increase within 1 Ma was observed at 14°14′S on the East Pacific Rise and was interpreted as filling of porosity with hydrothermally generated minerals [*Grevemeyer and Weigel*, 1997; *Grevemeyer and Bartetzko*, 2004]. Such off-axis hydrothermal precipitation is the common explanation for the increase of crustal velocities with age [*Carlson*, 1998]. An alteration front may create a depth below which pores have been sealed by alteration products [*Rohr et al.*, 1988; *Christeson et al.*, 2007]. This sealing depth may vary, if thin cracks are sealed near to the ridge axis and larger cracks are filled off axis [*Shaw*, 1994]. Another possible explanation for the off-axis velocity increase may be a porosity collapse with age, since off-axis crust is significantly older than crust in the median valley.

[50] The presence of an axial magma chamber, the abrupt velocity increase across the median valley bounding faults and the low-velocity anomalies below the Lucky Strike volcano have implications for fluid circulation in the subsurface. The Lucky Strike volcano hosts a high-temperature hydrothermal vent field [*Langmuir et al.*, 1997]. The heat source for the hydrothermal field is likely the axial magma chamber and the fluids discharge through a zone of increased porosities underneath the volcano, whereas zones of increased porosities underneath the western volcanic ridge show no evidence for high-temperature hydrothermal discharge. The location of the median valley bounding faults and the velocity increase indicate that at least some fluid recharge is occurring at the median valley bounding faults. The abrupt velocity change at the median valley bounding faults may indicate that fault activation increases hydrothermal activity facilitating secondary mineralization. While this simple circulation pattern is consistent with our observation, we cannot rule out a more complex circulation pattern. Lastly, our porosity estimates indicate that on the ridge axis significant porosity exists to the bottom of our model near the axial magma chamber. Applying the same method off axis shows that porosity is sealed porosity by ~1.75 km depth bsf. This observation indicates that off-axis hydrothermal circulation is either shallower than on the ridge axis or localized along major faults below the resolution of our velocity models.

[51] Finally, we observed an upper crustal azimuthal velocity anisotropy similar to the one observed at 35°N [*Barclay et al.*, 1998; *Dunn et al.*, 2005]. The azimuthal anisotropy appears to be slightly misaligned with the ridge axis. A possible explanations for this misalignment is a spreading axis that is not completely parallel to the ridge axis. Alternatively, the regional extensional stress field may not be perpendicular to the ridge axis. The direction of subsurface faults, fractures and cracks may differ slightly from the direction of the ridge axis. Most importantly however, axis parallel faulting and aligned cracks explain the upper crustal anisotropy observed above and are consistent with the extensional faulting observed on the seafloor of the median valley [*Escartín et al.*, 2008].

7. Conclusions

[52] A detailed 3-D model of the upper crust, obtained using closely spaced 3-D air gun shots to OBS, shows significant variations in upper crustal velocities beneath Lucky Strike volcano and its bounding axial valley. Our models show a low-velocity region within the median valley, low-velocity anomalies of the Lucky Strike volcano and an off-axis velocity increase of ~1 km/s over a distance of 8 km. The 3-D crustal velocity structure of the Lucky Strike Segment appears to be very similar to the one observed at 35°N [*Barclay et al.*, 1998; *Magde et al.*, 2000; *Dunn et al.*, 2005]. Our observations indicate a porosity decrease of 4%–11% with depth between 0.5 and 1.75 km bsf. Furthermore, we demonstrate a porosity decrease of 4%–9% at 0.5 km bsf depth and 1%–3% at a 1.75 km bsf depth over a distance of 8 km from the ridge axis (~0.7 Ma). Last, our velocity models require the presence of azimuthal anisotropy in the upper crust.

[53] The studies presented here help to understand the role of tectonic, magmatic and hydrothermal processes in defining the upper crustal seismic structure of the Lucky Strike Segment. It is important to realize that all three processes may be occurring synchronously and the observed porosity structure is likely effected by different processes. We favor a model, where upper crustal porosities are created by both magmatic accretion (lava–sheeted dike boundary) and active extensions (faults, fractures and fissures). The porosity variation with depth probably depends on both pore space collapse, hydrothermal alteration and a change of stress accommodation from distribution along minor faults, fractures and fissures to localization along major faults. Lastly, off-axis porosities are likely controlled by both hydrothermal precipitation and the aging of the crust.

Acknowledgments

[54] This work was made possible by the EU Marie Curie RTN Momarnet, Institut de Physique du Globe de Paris, CNRS/INSU, Ifremer, and the state of Portugal. The Earth Resource Laboratory of the Massachusetts Institute of Technology generously supported the final stages of the preparation of this manuscript. The OBS operations were assured by Laurent Béguery, Oualid Aouji, Carlos Corela, and Jose Duarte. Captain and crew of the French research vessel N/O L'*Atalante* helped to make this project a success. Last, this manuscript profited greatly from discussions with Mathilde Cannat, Juan-Pablo Canales, William Wilcock, and Ingo Grevemeyer. We thank two anonymous reviewers, who helped us to improve this manuscript. The Generic Mapping Tools and Seismic Unix were used for data processing and visualization.

References

Backus, G. (1965), Possible forms of seismic anisotropy of the uppermost mantle under oceans, *J. Geophys. Res.*, *70*(14), 3429–3439.

Barclay, A., D. Toomey, and S. Solomon (1998), Seismic structure and crustal magmatism at the Mid-Atlantic Ridge, 35°N, *J. Geophys. Res.*, *103*(B8), 17,827–17,844.

Barker, N. (2004), Electromagnetic investigation of the Lucky Strike seamount near 37°N, Mid-Atlantic Ridge, Ph.D. thesis, Univ. of Southampton, Southampton, U. K.

Becker, K. (1985), Large-scale electrical resistivity and bulk porosity of the upper oceanic crust, Deep Sea Drilling Project Hole 504B, Costa Rica Rift, *Initial Rep. Deep Sea Drill. Proj.*, *83*, 419–427, doi:10.2973/dsdp.proc.83.124.1985.

Becker, K. (1990), Large-scale electrical resistivity and bulk porosity of the upper oceanic crust at Hole 395A, *Proc. Ocean Drill. Program Sci. Results*, *106/109*, 205–212.

Becker, K., et al. (1982), In situ electrical resistivity and bulk porosity of the oceanic crust Cost Rica Rift, *Nature*, *300*, 594–598.

Becker, K., E. Davis, F. Spiess, and C. deMoustier (2004), Temperature and video logs from the upper oceanic crust, Holes 504B and 896(a), Costa Rica Rift flank: Implications for the permeability of upper oceanic crust, *Earth Planet. Sci. Lett.*, *222*, 887–896, doi:10.1016/j.epsl.2004.03.033.

Berge, P., J. Berryman, and B. Bonner (1993), Influence of microstructure on rock elastic properties, *Geophys. Res. Lett.*, *20*(23), 2619–2622.

Berryman, J., S. Pride, and H. Wang (2002), A differential scheme for elastic properties of rocks with dry or saturated cracks, *Geophys. J. Int.*, *151*, 597–611, doi:2002GeoJI.151..597B.

Boudier, F., A. Nicolas, B. Ildefonse, and D. Jousselin (1997), EPR microplates, a model for the Oman ophiolite, *Terra Nova*, *9*, 79–82.

Bratt, S., and G. Purdy (1984), Structure and variability of oceanic crust on the flanks of the East Pacific Rise between 11° and 13°N, *J. Geophys. Res.*, *89*(B7), 6111–6125.

Budiansky, B. (1965), On the elastic moduli of some heterogeneous materials, *J. Mech. Phys. Solids*, *13*, 223–227.

Buttkus, B. (2000), *Spectral Analysis and Filter Theory in Applied Geophysics*, 1st ed., Springer, Berlin.

Cannat, M., et al. (1999), Mid-Atlantic Ridge–Azores hotspot interactions: Along-axis migration of a hotspot-derived event of enhanced magmatism 10 to 4 Ma ago, *Earth Planet. Sci. Lett.*, *173*, 257–269.

Carlson, R. (1998), Seismic velocities in the uppermost oceanic crust: Age dependence and the fate of layer 2A, *J. Geophys. Res.*, *103*(B4), 7069–7077.

Carlson, R., and C. Herrick (1990), Densities and porosities in the oceanic crust and their variations with depth and age, *J. Geophys. Res.*, *95*(B6), 9153–9170.

Červený, V. (2001), *Seismic Ray Theory*, Cambridge Univ. Press, Cambridge, U. K.

Chapman, C. (2004), *Fundamentals of Seismic Wave Propagation*, Cambridge Univ. Press, New York.

Cheng, C., and M. Toksöz (1979), Inversion of seismic velocities for the pore aspect ratio spectrum of a rock, *J. Geophys. Res.*, *84*(B13), 7533–7543.

Christensen, N. (1984), Pore pressure and oceanic crustal seismic structure, *Geophys. J. R. Astron. Soc.*, *79*, 411–423.

Christeson, G., G. Purdy, and G. Fryer (1994), Seismic constraints on shallow crustal emplacement processes at the fast spreading East Pacific Rise, *J. Geophys. Res.*, *99*(B9), 17,957–17,973.

Christeson, G., G. Kent, G. Purdy, and R. Detrick (1996), Extrusive thickness variability at the East Pacific Rise, 9°–10°N: Constraints from seismic techniques, *J. Geophys. Res.*, *101*(B2), 2859–2873.

Christeson, G., K. McIntosh, and J. Karson (2007), Inconsistent correlation of layer 2A and lava layer thickness in oceanic crust, *Nature*, *445*, 418–421, doi:10.1038/nature05517.

Combier, V. (2007), Mid-ocean ridge processes: Insights from 3D reflection seismics at the 9°N OSC on the East Pacific Rise, and the Lucky Strike Volcano on the Mid-Atlantic Ridge, Ph.D. thesis, Inst. de Phys. du Globe de Paris, Paris.

Constable, S., R. Parker, and C. Constable (1987), Occam's inversion: A practical algorithm for generating smooth models from electromagnetic data, *Geophysics*, *52*(3), 289–300.

de Boor, C. (2001), *A Practical Guide to Splines*, *Appl. Math. Sci.*, vol. 27, Springer, New York.

deGroot Hedlin, C., and S. Constable (1990), Occam's inversion to generate smooth, two-dimensional models from magnetotelluric data, *Geophysics*, *55*(12), 1613–1624.

Detrick, R., P. Buhl, E. Vera, J. Mutter, J. Orcutt, J. Madsen, and T. Brocher (1987), Multi-channel seismic imaging of a crustal magma chamber along the East Pacific Rise, *Nature*, *326*, 35–41, doi:10.1038/326035a0.

Detrick, R., H. Needham, and V. Renard (1995), Gravity anomalies and crustal thickness variations along the Mid-Atlantic Ridge between 33°N and 40°N, *J. Geophys. Res.*, *100*(B3), 3767–3787.

Dougherty, M., and R. Stephen (1988), Seismic energy partitioning in laterally heterogeneous ocean crust, *Pure Appl. Geophys.*, *128*(1–2), 195–229.

Dunn, R., and D. Toomey (2001), Crack-induced seismic anisotropy in the oceanic crust across the East Pacific Rise (9°30′N), *Earth Planet. Sci. Lett.*, *189*, 9–17.

Dunn, R. A., V. Lekic, R. S. Detrick, and D. R. Toomey (2005), Three-dimensional seismic structure of the Mid-Atlantic Ridge (35°N): Evidence for focused melt supply and lower crustal dike injection, *J. Geophys. Res.*, *110*, B09101, doi:10.1029/2004JB003473.

Dusunur, D., J. Escartin, V. Combier, T. Seher, W. Crawford, M. Cannat, S. Singh, L. Matias, and J. Miranda (2009), Seismological constraints on the thermal structure along the Lucky Strike segment (Mid-Atlantic Ridge) and interaction of tectonic and magmatic processes around the magma chambers, *Mar. Geophys. Res.*, *30*(2), 105–120, doi:10.1007/s11001-009-9071-3.

Dziak, R. P., D. K. Smith, D. R. Bohnenstiehl, C. G. Fox, D. Desbruyeres, H. Matsumoto, M. Tolstoy, and D. J. Fornari (2004), Evidence of a recent magma dike intrusion at the slow spreading Lucky Strike segment, Mid-Atlantic Ridge, *J. Geophys. Res.*, *109*, B12102, doi:10.1029/2004JB003141.

Escartín, J., M. Cannat, G. Pouliquen, and A. Rabain (2001), Crustal thickness of V-shaped ridges south of the Azores: Interaction of the Mid-Atlantic Ridge (36°N–39°N) and the Azores hot spot, *J. Geophys. Res.*, *106*(B10), 21,719–21,735.

Escartín, J., et al. (2008), Globally aligned photomosaic of the Lucky Strike hydrothermal vent field (Mid-Atlantic Ridge, 37°18.5′N): Release of georeferenced data, mosaic construction, and viewing software, *Geochem. Geophys. Geosyst.*, *9*, Q12009, doi:10.1029/2008GC002204.

Fouquet, Y., H. Ondréas, J.-L. Charlou, J.-P. Donval, J. Radford-Knoery, I. Costa, N. Lourenço, and M. Tivey (1995), Atlantic lava lakes and hot vents, *Nature*, *377*(6546), 201.

Francheteau, J., R. Armijo, J. Cheminée, R. Hekinian, P. Lonsdale, and N. Blum (1990), 1 ma East Pacific Rise oceanic crust and uppermost mantle exposed by rifting in Hess Deep (equatorial Pacific Ocean), *Earth Planet. Sci. Lett*, *101*, 281–295.

Grevemeyer, I., and A. Bartetzko (2004), Hydrothermal aging of oceanic crust: Inferences from seismic refraction and borehole studies, in *Hydrogeology of the Oceanic Lithosphere*, pp. 128–150, Cambridge Univ. Press, Cambridge, U. K.

Grevemeyer, I., and W. Weigel (1997), Increase of seismic velocities in upper oceanic crust: The "superfast" spreading East Pacific Rise, *Geophys. Res. Lett.*, *24*(3), 217–220.

Harding, A. J., G. M. Kent, and J. A. Orcutt (1993), A multichannel seismic investigation of upper crustal structure at 9°N on the East Pacific Rise: Implications for crustal accretion, *J. Geophys. Res.*, *98*(B8), 13,925–13,944.

Hashin, Z., and S. Shtrikman (1963), A variational approach to the theory of the elastic behaviour of multiphase materials, *J. Mech. Phys. Solids*, *11*, 127–140.

Herron, T. (1982), Lava flow layer—East Pacific Rise, *Geophys. Res. Lett.*, *9*(1), 17–20.

Hill, R. (1965), A self-consistent mechanics of composite materials, *J. Mech. Phys. Solids*, *13*, 213–222.

Hobro, J. (1999), Three-dimensional tomographic inversion of combined reflection and refraction seismic traveltime data, Ph.D. thesis, Univ. of Cambridge, Cambridge, U. K.

Hobro, J., S. Singh, and T. Minshull (2003), Three-dimensional tomographic inversion of combined reflection and refraction seismic traveltime data, *Geophys. J. Int.*, *152*, 79–93.

Hooft, E., H. Schouten, and R. Detrick (1996), Constraining crustal emplacement processes from the variation in seismic layer 2A thickness at the East Pacific Rise, *Earth Planet. Sci. Lett.*, *142*, 289–309.

Hooft, E., R. Detrick, D. Toomey, J. Collins, and J. Lin (2000), Crustal thickness and structure along three contrasting spreading segments of the Mid-Atlantic Ridge, 33.5°–35°N, *J. Geophys. Res.*, *105*(B4), 8205–8226.

Hornby, B., L. Schwartz, and J. Hudson (1994), Anisotropic effective-medium modeling of the elastic properties of shales, *Geophysics*, *59*(10), 1570–1583.

Houtz, R., and E. Ewing (1976), Upper crustal structure as a function of plate age, *J. Geophys. Res.*, *81*(14), 2490–2498.

Humphris, S., D. Fornari, D. Scheirer, C. German, and L. Parson (2002), Geotectonic setting of hydrothermal activity on the summit of Lucky Strike Seamount (37°17′N, Mid-Atlantic Ridge), *Geochem. Geophys. Geosyst.*, *3*(8), 1049, doi:10.1029/2001GC000284.

Hung, S.-H., Y. Shen, and L.-Y. Chiao (2004), Imaging seismic velocity structure beneath the Iceland hot spot: A finite frequency approach, *J. Geophys. Res.*, *109*, B08305, doi:10.1029/2003JB002889.

Hussenoeder, S., R. Detrick, G. Kent, H. Schouten, and A. Harding (2002a), Fine-scale seismic structure of young upper crust at 17°20′S on the fast spreading East Pacific Rise, *J. Geophys. Res.*, *107*(B8), 2158, doi:10.1029/2001JB001688.

Hussenoeder, S., G. Kent, and R. Detrick (2002b), Upper crustal seismic structure of the slow spreading Mid-Atlantic Ridge, 35°N: Constraints on volcanic emplacement processes, *J. Geophys. Res.*, *107*(B8), 2156, doi:10.1029/2001JB001691.

Ito, G. (2001), Reykjanes 'V'-shaped ridges originating from a pulsing and dehydrating mantle plume, *Nature*, *411*, 681–684.

Jacobsen, R. (1992), Impact of crustal evolution on changes of the seismic properties of the uppermost ocean crust, *Rev. Geophys.*, *30*(1), 23–42.

Jakobsen, M., J. Hudson, T. Minshull, and T. Singh (2000), Elastic properties of hydrate-bearing sediments using effective medium theory, *J. Geophys. Res.*, *105*(B1), 561–577.

Jean-Baptiste, P., H. Bougault, A. Vangriesheim, J. L. Charlou, J. Radford-Knoery, Y. Fouquet, D. Needham, and C. German (1998), Mantle ^{3}He in hydrothermal vents and plume of the Lucky Strike site (MAR 37°17′N) and associated geothermal heat flux, *Earth Planet. Sci. Lett.*, *157*, 69–77.

Johnston, J., and N. Christensen (1997), Seismic properties of layer 2 basalts, *Geophys. J. Int.*, *128*, 285–300.

Johnston, J., G. Fryer, and N. Christensen (1995), Velocity-porosity relationships of basalts from the East Pacific Rise, *Proc. Ocean Drill. Program Sci. Results*, *142*, 51–59.

Karson, J. (1998), Internal structure of oceanic lithosphere: A perspective from tectonic windows, in *Faulting and Magmatism at Mid-Ocean Ridges*, *Geophys. Monogr. Ser.*, vol. 106, edited by W. R. Buck et al., pp. 177–218, AGU, Washington, D. C.

Karson, J., E. Klein, S. Hurst, C. Lee, P. Rivizzigno, D. Curewitz, A. Morris, and Hess Deep '99 Scientific Party (2002), Structure of uppermost fast-spread oceanic crust exposed at the Hess Deep Rift: Implications for subaxial processes at the East Pacific Rise, *Geochem. Geophys. Geosyst.*, *3*(1), 1002, doi:10.1029/2001GC000155.

Kent, G., A. Harding, and J. Orcutt (1993), Distribution of magma beneath the East Pacific Rise between the Clipperton transform and 9°17′N Deval from forward modeling of common depth point data, *J. Geophys. Res.*, *98*(B8), 13,945–13,969.

Kissling, E. (1988), Geotomography with local earthquake data, *Rev. Geophys.*, *26*(4), 659–698.

Langmuir, C., et al. (1997), Hydrothermal vents near a mantle hot spot: The Lucky Strike vent field at 37°N on the Mid-Atlantic Ridge, *Earth Planet. Sci. Lett.*, *148*, 69–91.

Lévêque, J.-L., L. Rivera, and G. Wittlinger (1993), On the use of the checker-board test to assess the resolution of tomographic inversions, *Geophys. J. Int.*, *115*, 313–318.

Lucazeau, F., A. Bonneville, J. Escartin, R. P. Von Herzen, P. Gouze, H. Carton, M. Cannat, V. Vidal, and C. Adam (2006), Heat flow variations on a slowly accreting ridge: Constraints on the hydrothermal and conductive cooling for the Lucky Strike segment (Mid-Atlantic Ridge, 37°N), *Geochem. Geophys. Geosyst.*, *7*, Q07011, doi:10.1029/2005GC001178.

Magde, L., A. Barclay, D. Toomey, R. Detrick, and J. Collins (2000), Crustal magma plumbing within a segment of the Mid-Atlantic Ridge, 35°N, *Earth Planet. Sci. Lett.*, *175*, 55–67.

Mainprice, D. (1997), Modeling the anisotropic seismic properties of partially molten rocks found at mid-ocean ridges, *Tectonophysics*, *279*, 161–179.

Miranda, J. M., J. F. Luis, N. Lourenço, and F. M. Santos (2005), Identification of the magnetization low of the Lucky Strike hydrothermal vent using surface magnetic data, *J. Geophys. Res.*, *110*, B04103, doi:10.1029/2004JB003085.

Moreira, M., and C.-J. Allègre (2002), Rare gas systematics on Mid Atlantic Ridge (37–40°N), *Earth Planet. Sci. Lett.*, *198*, 401–416.

Müller, R., W. Roest, J.-Y. Royer, L. Gahagan, and J. Sclater (1997), Digital isochrons of the world's ocean floor, *J. Geophys. Res.*, *102*(B2), 3211–3214.

Nicolas, A., and F. Boudier (1995), Mapping oceanic ridge segments in Oman ophiolite, *J. Geophys. Res.*, *100*(B4), 6197–6197.

Nicolas, A., I. Reuber, and K. Benn (1988), A new magma chamber model based on structural studies in the Oman ophiolite, *Tectonophysics*, *151*, 87–105.

Nisbet, E., and C. Fowler (1978), The Mid-Atlantic Ridge at 37 and 45°N: Some geophysical and petrological constraints, *Geophys. J. R. Astron. Soc.*, *54*(3), 631–660.

Norris, A. (1985), A differential scheme for the effective moduli of composites, *Mech. Mater.*, *4*(1), 1–16, doi:10.1016/0167-6636(85)90002-X.

Nur, A., G. Mavko, J. Dvorkin, and D. Galmudi (1998), Critical porosity: A key to relating physical properties to porosity in rocks, *Leading Edge*, *17*, 357–362, doi:10.1190/1.1437977.

Ondréas, H., Y. Fouquet, M. Voisset, and J. Radford-Knoery (1997), Detailed study of three contiguous segments of the Mid-Atlantic Ridge, south of the Azores (37°N to 38°30′N), using acoustic imaging coupled with submersible observations, *Mar. Geophys. Res.*, *19*, 231–255.

Ondréas, H., M. Cannat, Y. Fouquet, A. Normand, P. Sarradin, and J. Sarrazin (2009), Recent volcanic events and the distribution of hydrothermal venting at the Lucky Strike hydrothermal field, Mid-Atlantic Ridge, *Geochem. Geophys. Geosyst.*, *10*, Q02006, doi:10.1029/2008GC002171.

Parson, L., E. Gràcia, D. Coller, C. German, and D. Needham (2000), Second-order segmentation: The relationship between volcanism and tectonism at the MAR, 38°N–35°40′N, *Earth Planet. Sci. Lett.*, *178*, 231–251.

Press, W., B. Flannery, S. A. Teukolsky, and W. Vetterling (1992), *Numerical Recipes in FORTRAN 77: The Art of Scientific Computing*, vol. 1, 2nd ed., Cambridge Univ. Press, Cambridge, U. K.

Purdy, G., and R. Detrick (1986), Crustal structure of the Mid-Atlantic Ridge at 23°N from seismic refraction studies, *J. Geophys. Res.*, *91*(B3), 3739–3762.

Rohr, K., B. Milkereit, and C. Yorath (1988), Asymmetric deep crustal structure across the Juan de Fuca Ridge, *Geology*, *16*, 533–537.

Schouten, H., M. Tivey, D. Fornari, and J. Cochran (1999), Central anomaly magnetization high: Constraints on the volcanic construction and architecture of seismic layer 2A at a fast spreading mid-ocean ridge, the EPR at 9°30′–50′N, *Earth Planet. Sci. Lett.*, *169*, 37–50.

Seher, T., W. C. Crawford, S. C. Singh, M. Cannat, V. Combier, and D. Dusunur (2010), Crustal velocity structure of the Lucky Strike segment of the Mid-Atlantic Ridge at 37°N from seismic refraction measurements, *J. Geophys. Res.*, *115*, B03103, doi:10.1029/2009JB006650.

Shaw, P. (1994), Age variations of oceanic crust Poisson's ratio: Inversion and a porosity evolution model, *J. Geophys. Res.*, *99*(B2), 3057–3066.

Shaw, P., and J. Orcutt (1985), Waveform inversion of seismic refraction data and applications to young Pacific crust, *Geophys. J. R. Astron. Soc.*, *82*, 375–414.

Shearer, P., and J. Orcutt (1986), Compressional and shear wave anisotropy in the oceanic lithosphere—The Ngendei seismic refraction experiment, *Geophys. J. R. Astron. Soc.*, *87*, 967–1003.

Singh, S., W. Crawford, H. Carton, T. Seher, V. Combier, M. Cannat, J. Canales, D. Düsünür, J. Escartin, and J. Miranda (2006), Discovery of a magma chamber and faults beneath a Mid-Atlantic Ridge hydrothermal field, *Nature*, *442*(31), 1029–1032, doi:10.1038/nature05105.

Sinton, J., and R. Detrick (1992), Mid-ocean ridge magma chambers, *J. Geophys. Res.*, *97*(B1), 197–216.

Smith, D., and J. Cann (1993), Building the crust at the Mid-Atlantic Ridge, *Nature*, *365*, 707–715, doi:10.1038/365707a0.

Stephen, R. (1985), Seismic anisotropy in the upper oceanic crust, *J. Geophys. Res.*, *90*(B13), 11,383–11,396.

Tarantola, A. (2005), *Inverse Problem Theory and Methods for Model Parameter Estimation*, Soc. for Ind. and Appl. Math., Philadelphia, Pa.

Taylor, M., and S. Singh (2002), Composition and microstructure of magma bodies from effective medium theory, *Geophys. J. Int.*, *149*, 15–21.

Telford, W., L. Geldart, and R. Sheriff (1990), *Applied Geophysics*, Cambridge Univ. Press, Cambridge, U. K.

Thibaud, R., P. Gente, and M. Maia (1998), A systematic analysis of the Mid-Atlantic Ridge morphology and gravity between 15°N and 40°N: Constraints of the thermal structure, *J. Geophys. Res.*, *103*(B10), 24,223–24,243.

Tong, C. H., C. Lana, R. S. White, M. R. Warner, and ARAD Working Group (2005), Subsurface tectonic structure between overlapping mid-ocean ridge segments, *Geology*, *33*(5), 409–412, doi:10.1130/G21245.1.

Toomey, D., G. Purdy, S. Solomon, and W. Wilcock (1990), The three-dimensional seismic velocity structure of the East Pacific Rise near latitude 9°30′N, *Nature*, *347*, 639–645.

Virieux, J., and V. Farra (1991), Ray tracing in 3-D complex isotropic media: An analysis of the problem, *Geophysics*, *58* (12), 2057–2069.

Wepfer, W., and N. Christensen (1991), A seismic velocity-confining pressure relation, with applications, *Int. J. Rock Mech. Min. Sci. Geomech. Abstr.*, *28*(5), 451–456.

White, R., and R. Whitmarsh (1984), An investigation of seismic anisotropy due to cracks in the upper oceanic crust at 45°N, Mid-Atlantic Ridge, *Geophys. J. R. Astron. Soc.*, *79*(2), 439–467.

Yang, T., Y. Shen, S. van der Lee, S. Solomon, and S.-H. Hung (2006), Upper mantle structure beneath the Azores hotspot from finite-frequency seismic tomography, *Earth Planet. Sci. Lett.*, *250*, 11–26, doi:10.1016/j.epsl.2006.07.031.

Zelt, C. (1998), Lateral velocity resolution from three-dimensional seismic refraction data, *Geophys. J. Int.*, *135*, 1101–1112.

Zelt, C. (1999), Modelling strategies and model assessment for wide-angle seismic traveltime data, *Geophys. J. Int.*, *139*, 183–204.